PERGAMON

International Journal of Heat and Mass Transfer 43 (2000) 589–610

International Journal of HEAT and MASS TRANSFER

www.elsevier.com/locate/ijhmt

Linear stability of mixed convection flows in horizontal rectangular channels of finite transversal extension heated from below

X. Nicolas[a,*], J.-M. Luijkx[b], J.-K. Platten[b]

[a]*Institut de Mécanique des Fluides, UMR CNRS/INP-UPS 5502, Université Paul Sabatier, UFR MIG, 118 route de Narbonne, 31062 Toulouse Cedex, France*

[b]*Laboratoire de Chimie Générale, Faculté de Médecine, Université de Mons-Hainaut, 7000 Mons, Belgium*

Received 26 June 1998; accepted 15 March 1999

Abstract

We present a study of the linear hydrodynamic stability of purely conductive Poiseuille flow in three-dimensional horizontal rectangular channels uniformly heated from below. Its originality is to modellize the flow using realistic conditions on all the boundaries of the channel, in particular, no-slip conditions on the vertical lateral boundaries. The aim of this paper is to provide quantitative results for the values of the critical dimensionless parameters. When the Rayleigh number Ra is higher than the critical value Ra^*, the instabilities are shown to be three-dimensional horseshoe-shaped transversal rolls for Reynolds numbers Re smaller than the critical value Re^*, and longitudinal rolls for $Re > Re^*$. The results are given for a wide range of the Prandtl number ($10^{-6} \leq Pr \leq 10^5$) and of the transversal aspect ratio B of the duct ($0.1 \leq B \leq 5.4$ and $B \to \infty$).

1. Introduction

The mixed convection flows in horizontal rectangular channels heated from below are also called Poiseuille–Bénard flows (PBF). Their study has given rise to numerous works because this flow remains relatively complex, with some aspects misunderstood. This is partly due to the fact that the PBF is characterized by four dimensionless parameters (Ra, Re, Pr, B), and several flow patterns.

Some of the papers on the PBF are of practical or technological interest: e.g. in meteorology [1,2], in the cooling of electronic equipment [3–5], or in the production of thin films in chemical vapour deposition reactors [6–8]. Other papers aim at understanding the two main thermoconvective roll patterns of this flow (the transversal rolls and the longitudinal rolls) and their stability [9–16]. Fig. 1 shows 'transversal rolls' and 'longitudinal rolls', subsequently noted $R_\perp$ and $R_{//}$, respectively.

A bibliographical summary of the linear stability studies on the transitions between the basic flow and the $R_{//}$ or the $R_\perp$ in the PBF is presented in Table 1, together with the form of the normal modes and the type of the thermoconvective rolls observed just beyond the instability threshold. In those papers, f represents any perturbation, k_x and k_y are the wave numbers in the axial and transversal directions, respectively, and $\sigma = \sigma_r + i\sigma_i$ is the complex time amplification coefficient.

* Corresponding author. Present address: Laboratoire MSNPT, Université de Marne-la-Vallée, Bât. Lavoisier, Cité Descartes, 5 Boulevard Descartes, Champs-sur-Marne, 77454 Marne-la-Vallée Cedex 2, France.

0017-9310/00/$ - see front matter
PII: S0017-9310(99)00099-X

Nomenclature

B	transversal aspect ratio of the duct, l/h
g	gravitational acceleration
h	channel height in z-direction
k_x, k_y	wave numbers in x- and y-directions
$\mathbf{k}$	upward vertical unit vector
l	channel width in y-direction
LDA	laser Doppler anemometry
$\mathscr{L}$	eigenvalue problem
P	dimensional and dimensionless pressure
PBF	Poiseuille–Bénard flow
Pr	Prandtl number, ν^0/α^0
$R_\perp$	transversal rolls
$R_{//}$	longitudinal rolls
Ra	Rayleigh number, $g\beta^0(T_h-T_c)h^3/\nu^0\alpha^0$
Ra^*	critical Rayleigh number, $\min(Ra^*_\perp, Ra^*_{//})$
$Ra^*_\perp$	critical Rayleigh number for the appearance of transversal rolls
$Ra^*_{//}$	critical Rayleigh number for the appearance of longitudinal rolls
$Ra^{conv}_\perp$	critical Rayleigh number between convective and absolute instability domains for transversal rolls
Re	Reynolds number, $\langle\bar{U}\rangle h/\nu^0$
Re^*	critical Reynolds number corresponding to the transition between transversal and longitudinal rolls
S	size of the eigenvalue problem square matrices (I MAX $\times$ J MAX + K MAX $\times$ L MAX + M MAX $\times$ N MAX)^2
t	dimensionless time
T	dimensional and dimensionless fluid temperature
T_c, T_h	temperature of the cold top and hot bottom plates of the channel
u, v, w	dimensionless horizontal, transversal and vertical velocity components
U, V, W	dimensional horizontal, transversal and vertical velocity components
U^0	average velocity of the two-dimensional Poiseuille flow
$\langle\bar{U}\rangle$	average velocity of the three-dimensional basic flow
$\mathbf{V}$	velocity vector (U, V, W)
Vr	transversal roll velocity
x, y, z	dimensionless axial, spanwise and vertical coordinates.

Greek symbols

α	thermal diffusivity
β	thermal expansion coefficient
λ	dimensionless transversal roll wavelength
ν	kinematic viscosity
ρ	mass per unit volume
σ	complex time amplification coefficient, $\sigma_r + i\sigma_i$
τ	dimensionless transversal roll time period.

Subscripts

i, r	imaginary and real part of complex numbers.

Superscripts

E, O	even, odd
max	maximum
0	reference state or average value of the flow
*	critical value
-	basic state for the linear stability study
′	infinitesimal perturbations
ˆ	normal mode amplitudes.

The two first linear stability studies of the PBF by Velte [17] and Sani [18] provide qualitative results about the growth of $R_{//}$ in finite lateral extension ducts. In particular, the critical Rayleigh number $Ra^*_{//}$, corresponding to the transition between the basic flow and the $R_{//}$, is shown to increase when B decreases. Mori and Uchida [19], considering infinite lateral extension ducts, focus on $R_{//}$. The critical Rayleigh number $Ra^*_{//}$ and the critical wave number k^*_y are shown to be independent of Re ($Ra^*_{//}=1708$ and $k^*_y=3.13$). The linear theory developed by Gage and Reid [20] considers transversal, longitudinal or oblique rolls in infinite lateral extension ducts, but only at $Pr = 1$. It has been generalized to all Prandtl numbers in the case of $R_\perp$ by Platten [21], using a restricted variational technique. However, to our knowledge, the most comprehensive linear stability study of the PBF is Luijkx's work [9]. It provides precise quantitative results for a wide range of the dimensionless parameters of the flow, both for channels of finite and infinite lateral extension.

In Fig. 2, we remind the reader of the stability diagram when $B \to \infty$. At $Re = 0$, the basic flow becomes unstable at $Ra = 1708$. The critical Rayleigh number $Ra^*_{//}$, corresponding to perturbations of the form $A(z)\,e^{ik_y y}$, is independent of Re ($Ra^*_{//}=1708$), whereas the critical Rayleigh number $Ra^*_\perp$ for the appearance of the $R_\perp$ (perturbations of the form $A(z)\,e^{i(k_x x+\sigma_i t)}$),

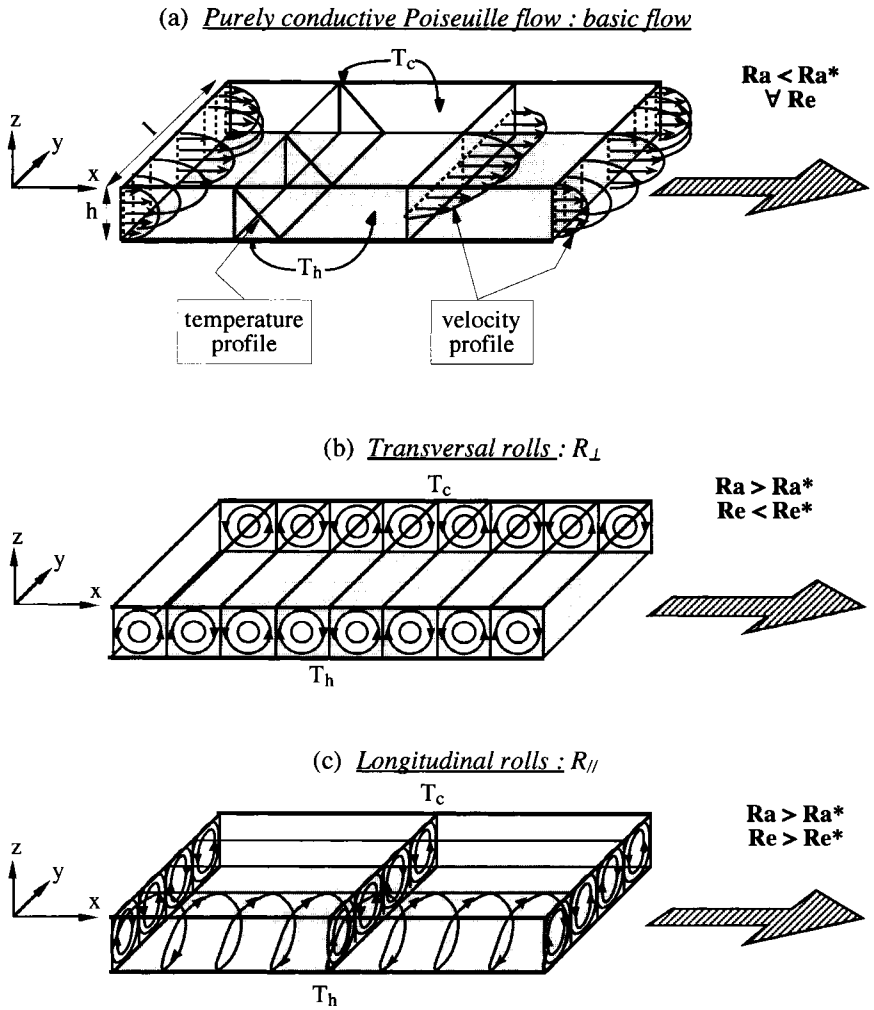

Fig. 1. Schematic representation of the three main flow patterns of the Poiseuille–Bénard flow.

increases with Re. Lastly, for any perturbations of the form $A(z)\,e^{i(k_x x+k_y y+\sigma_i t)}$, Squire's theorem [22] may be invoked and produces curve 2 [23]. Therefore, without a lateral confinement and whatever Re, the basic flow becomes linearly unstable towards the $R_{//}$ at $Ra^*=1708$.

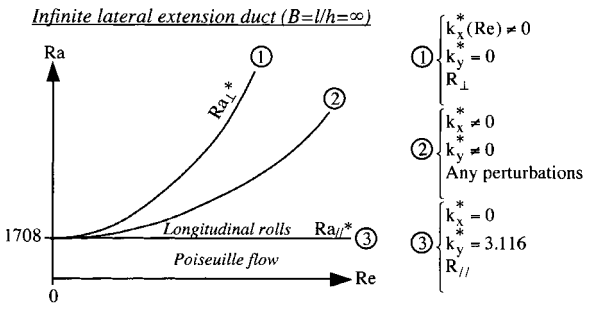

Fig. 2. Linear stability diagram of the Poiseuille–Bénard flow in infinite lateral extension ducts; three types of perturbations are considered.

Qualitative results for channels of finite transversal extension (see Fig. 3) are briefly presented in [23,24], together with the existence of the two types of rolls. The aim of this paper is to provide a *quantitative* parametric study of $Ra^*=Ra^*(Re, Pr, B)$. Fig. 3 shows that the lateral confinement has two effects: first, the basic flow is stabilized, since $Ra^*=\min(Ra^*_{//}, Ra^*_{\perp})$ increases when B decreases; secondly, at small Re ($Re < Re^*$), $R_{\perp}$ are favoured by the presence of the lateral vertical walls. On the other hand, when $Re > Re^*$, the average flow aligns the rolls parallel to the axis of the channel. Finally, it can be noted that $Ra^*_{\perp}$ is an increasing function of the Prandtl number Pr, while $Ra^*_{//}$ is independent of Pr. Therefore, Re^* decreases when Pr increases. Thus, $Ra^*_{//}=Ra^*_{//}(B)$,

Table 1
The different linear stability studies concerning the fully-established Poiseuille–Bénard flow

References	Transversal aspect ratio	*Pr*	*Re*	Form of the perturbations (normal modes)	Concerned roll patterns
Velte [17]	Finite $B = 1$	Qualitative study		$f(y, z, t) = A(y, z)\, e^{\sigma_r t}$ with $\sigma_r = 0$	$R_{//}$
Sani [18]	Finite	Qualitative study		$f(y, z, t) = A(y, z)\, e^{\sigma_r t}$ with $\sigma_r = 0$	$R_{//}$
Mori and Uchida [19]	Infinite	0.7	230–570	$f(y, z, t) = A(z) \cos(k_y y)\, e^{\sigma_r t}$ with $\sigma_r = 0$	$R_{//}$
Gage and Reid [20]	Infinite	1	$10–10^6$	$f(x, y, z, t) = A(z)\, e^{i(k_x x + k_y y + \sigma_i t)}\, e^{\sigma_r t}$ with $\sigma_r = 0$	$R_{//}$, $R_\perp$, R_{oblique}
Platten [21]	Infinite	0.7–7	0–6700	$f(x, z, t) = A(z)\, e^{i(k_x x + \sigma_i t)}\, e^{\sigma_r t}$ with $\sigma_r = 0$	$R_\perp$
Luijkx et al. [24]	Finite	Qualitative study			$R_{//}$, $R_\perp$
Luijkx [9]	Infinite	0–453	0–8000	$f(x, y, z, t) = A(z)\, e^{i(k_x x + k_y y + \sigma_i t)}\, e^{\sigma_r t}$ with $\sigma_r = 0$	$R_{//}$, $R_\perp$
Luijkx [9]	Finite $0 \le B \le 5.4$	$0–10^5$	0–1770	$f(x, y, z, t) = A(y, z)\, e^{i(k_x x + \sigma_i t)}\, e^{\sigma_r t}$ with $\sigma_r = 0$	$R_{//}$, $R_\perp$
Platten and Legros [23]	Infinite	7	0–100	$f(x, y, z, t) = A(z)\, e^{i(k_x x + k_y y + \sigma_i t)}\, e^{\sigma_r t}$ with $\sigma_r = 0$	$R_{//}$, $R_\perp$
Platten and Legros [23]	Finite $B = 2$ and 5.2	1–453	0–10	$f(x, y, z, t) = A(y, z)\, e^{i(k_x x + \sigma_i t)}\, e^{\sigma_r t}$ with $\sigma_r = 0$	$R_{//}$, $R_\perp$

$Ra_\perp^* = Ra_\perp^*(Re,\ Pr,\ B)$, and $Re^* = Re^*(Pr,\ B)$. The main goal of the present paper is to give numerical values for these functions.

Recent experimental [14,25], theoretical [26,27] and numerical [28–30] studies have shown the existence of complex flow configurations like superpositions of $R_\perp$ and $R_{//}$ [25,28,29], intermittent patterns [14], oblique rolls [30], or horseshoe patterns [28]. Other recent numerical works [31,32] have used the PBF as a test-case to study the influence of the open inlet and outlet boundary conditions of the computational domains, on the development of the thermoconvective patterns.

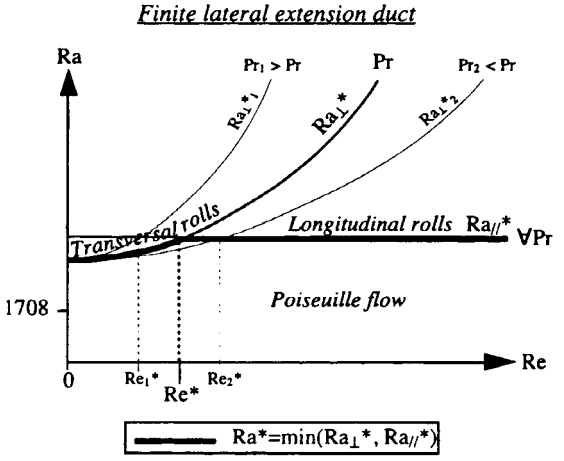

Fig. 3. Linear stability diagram of the Poiseuille–Bénard flow in finite lateral extension ducts; the influence of the Prandtl number is represented.

Finally, studies [15,16,27,33] have shown that the notions of convective and absolute instability is a fundamental point to properly determine the transition thresholds between the basic flow and the different types of thermoconvective flows. Using a weakly non-linear theory based on a Ginzburg–Landau equation Müller et al. [16] have determined the transition curve $Ra_\perp^{\text{conv}}$ between the convective and absolute instability zones for the $R_\perp$. Ouazzani et al. [15], experimentally, and Nicolas et al. [33], numerically, have shown that the transition between the basic flow and the $R_\perp$ corresponds to the curve $Ra_\perp^{\text{conv}}$, provided that the flow is not continuously perturbated near the inlet. However, if the flow is continuously perturbated near the inlet (e.g. mechanically by some vibrating device), the experiments should coincide with $Ra_\perp^*$, and not with $Ra_\perp^{\text{conv}}$. Therefore, the knowledge of $Ra_\perp^*(Re)$ is also of interest for future experiments. Finally, the Ginzburg–Landau equation used by Müller et al. [16] is a mono-dimensional model-equation allowing one to describe the space and time modulations of the amplitude of a perturbation in a *bi-dimensional* flow; but, it cannot take into account the effect of the lateral confinement of the duct. So, at the end of this paper, we will compare the results of the two-dimensional (2-D) weakly non-linear studies with the results of the three-dimensional (3-D) linear stability theory. As a general rule, the results obtained by the linear theory will be discussed in light of other recent results of the literature.

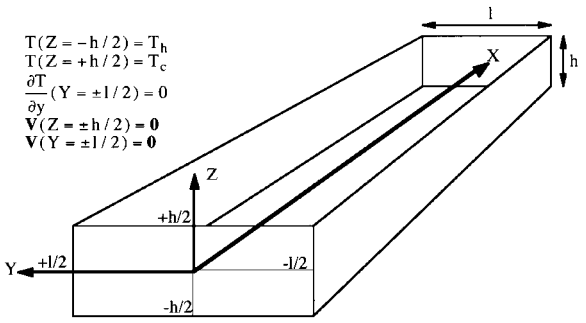

Fig. 4. System of coordinates and boundary conditions for the finite lateral extension duct.

2. Theoretical analysis

The linear stability analysis of the Rayleigh–Bénard problem ($Re = 0$) in ducts of finite lateral extension, has already been studied by Luijkx and Platten [34] and Platten and Legros [23]. In this paper ($Re \neq 0$), we consider the flow of a pure incompressible Newtonian fluid, in an infinite horizontal channel of rectangular cross section. Pure Poiseuille flow is driven by a pressure gradient $\partial P/\partial x$. The geometry and the different boundary conditions are presented in Fig. 4. The horizontal boundaries ($Z = \pm h/2$), rigid and perfectly heat conducting, are maintained at constant temperatures, the bottom plate being heated ($T = T_h$) and the top plate cooled ($T = T_c$). The lateral boundaries ($Y = \pm 1/2$) are also rigid but perfectly heat insulating. The governing equations in the Boussinesq approximation are:

$$\begin{cases} \nabla \cdot \mathbf{V} = 0 \\ \dfrac{\partial \mathbf{V}}{\partial t} + (\mathbf{V} \cdot \nabla)\mathbf{V} = -\dfrac{1}{\rho^0}\nabla P + \nu^0 \nabla^2 \mathbf{V} + \beta^0 (T - T^0) g \mathbf{k} \\ \dfrac{\partial T}{\partial t} + \mathbf{V} \cdot \nabla T = \alpha^0 \nabla^2 T \end{cases} \tag{1}$$

where ρ^0, ν^0, β^0 and α^0 are defined at the average temperature of the flow $T^0 = (T_h + T_c)/2$.

2.1. Computation of the analytical form of the basic flow

We seek a basic state $\bar{\mathbf{V}} = (\bar{U}(Y, Z), 0, 0)$, $\bar{T} = \bar{T}(Z)$ and $\bar{P} = \bar{P}(X, Z)$ given by:

$$\begin{cases} \dfrac{\partial \bar{P}}{\partial X} = \rho^0 \nu^0 \left(\dfrac{\partial^2 \bar{U}}{\partial Y^2} + \dfrac{\partial^2 \bar{U}}{\partial Z^2} \right) \\ \dfrac{\partial \bar{P}}{\partial Z} = \rho^0 \beta^0 g (\bar{T} - T^0) \\ \bar{T} = T^0 - \dfrac{(T_h - T_c)}{h} Z \end{cases} \tag{2}$$

We introduce dimensionless variables by the following transformations:

$$X \to hx \quad \bar{U} \to U^0 \bar{u}$$

$$Y \to ly \quad \bar{T} - T^0 \to (T_h - T_c)\bar{T} \tag{3}$$

$$Z \to hz \quad \bar{P} \to \frac{\alpha^0 \nu^0 \rho^0}{h^2} \bar{P}$$

where the scaling factor $U^0 = (K_P h^2 / 12 \rho^0 \nu^0)$ represents the average velocity of the 2-D Poiseuille flow, induced by the horizontal pressure gradient $-K_P = (\partial \bar{P}/\partial X)$.

Thus, the dimensionless temperature profile is $\bar{T}(z) = -z$ and the dimensionless form of the basic flow $\bar{u}(y, z)$ satisfies the following equation, in which $B = l/h$ is the transversal aspect ratio of the channel:

$$\frac{1}{B^2}\frac{\partial^2 \bar{u}}{\partial y^2} + \frac{\partial^2 \bar{u}}{\partial z^2} = -12 \quad \text{with} \begin{cases} \bar{u}(y = \pm 1/2) = 0 \\ \bar{u}(z = \pm 1/2) = 0 \end{cases} \tag{4}$$

The solution of (4) is searched in the form $u(y, z) = 6(1/4 - z^2) + P(y)Q(z)$. The term $6(1/4 - z^2)$ corresponds to the profile of the 2-D Poiseuille flow with unit average value. Thus, Eq. (4) gives:

$$\begin{cases} \dfrac{\mathrm{d}^2 P(y)}{\mathrm{d}y^2} - K B^2 P(y) = 0 \\ \dfrac{\mathrm{d}^2 Q(z)}{\mathrm{d}z^2} + K Q(z) = 0 \end{cases} \tag{5}$$

where K is the positive separation constant. The solution of (5) is:

$$\begin{cases} P(y) = A_1 \ \mathrm{ch}(\sqrt{K} B y) + A_2 \ \mathrm{sh}(\sqrt{K} B y) \\ Q(z) = C_1 \ \cos(\sqrt{K} z) + C_2 \ \sin(\sqrt{K} z) \end{cases} \tag{6}$$

where A_1, A_2, C_1 and C_2 are the four integration constants. Remember that $\bar{u}(y, z)$ has to be symmetrical about the horizontal and vertical midplanes, implying $A_2 = 0$ and $C_2 = 0$. The application of $\bar{u}(z = 1/2) = 0$ gives $\sqrt{K} = (2n + 1)\pi$, with $n \in Z$. Therefore, the general form of the solution is:

$$\bar{u}(y, z) = 6\left(\frac{1}{4} - z^2\right) + \sum_{n=0}^{\infty} A_n \ \mathrm{ch}((2n + 1)\pi B y) \cos((2n + 1)\pi z) \tag{7}$$

The constants A_n are determined by the last boundary condition $\bar{u}(y = 1/2) = 0$ which is still to be satisfied, i.e.:

$$\sum_{n=0}^{\infty} A_n \operatorname{ch}\left(\left(n+\frac{1}{2}\right)\pi B\right)\cos((2n+1)\pi z) = 6\left(z^2-\frac{1}{4}\right) \tag{8}$$

Multiplying the two sides of (8) by $\cos(m\pi z/2)$, with $m \in Z$, integrating for $-1/2 \le z \le 1/2$, and using the orthogonality relations, we get:

$$A_n = \frac{48(-1)^{n+1}}{(2n+1)^3\pi^3 \operatorname{ch}\left(\left(n+\frac{1}{2}\right)\pi B\right)} \tag{9}$$

Finally, the reduced velocity profile of the basic flow is:

$$\bar{u}(y,z) = 6\left(\frac{1}{4}-z^2\right) + \frac{48}{\pi^3}\sum_{n=0}^{\infty}\frac{(-1)^{n+1}\operatorname{ch}((2n+1)\pi B y)\cos((2n+1)\pi z)}{(2n+1)^3\operatorname{ch}\left(\left(n+\frac{1}{2}\right)\pi B\right)} \tag{10}$$

The dimensional average velocity $\langle \bar{U} \rangle$ and the dimensional maximum velocity $\bar{U}^{\max}$ of the 3-D basic flow $\bar{u}(y,z)$, which are functions of the aspect ratio of the duct, are listed in Table 2.

2.2. Perturbation equations

The dimensionless and linearized equations for infinitesimal disturbances (denoted by $'$) read:

$$\frac{\partial u'}{\partial x}+\frac{1}{B^2}\frac{\partial v'}{\partial y}+\frac{\partial w'}{\partial z}=0 \tag{11}$$

Table 2
Average and maximum velocities of the 3-D basic flow as a function of the aspect ratio of the duct

B	$\langle \bar{U} \rangle$	$\bar{U}_{\max}$
0.1	$0.009370U^0$	$0.015000U^0$
0.5	$0.171511U^0$	$0.341615U^0$
1	$0.421731U^0$	$0.884056U^0$
2	$0.686045U^0$	$1.366462U^0$
3	$0.789951U^0$	$1.472189U^0$
3.63[a]	$0.826382U^0$	$1.489661U^0$
4	$0.842439U^0$	$1.494218U^0$
5	$0.873950U^0$	$1.498798U^0$
10	$0.936975U^0$	$1.499999U^0$
100	$0.993698U^0$	$1.5U^0$
∞	U^0	$1.5U^0$

[a] Corresponds to the experiments of Ouazzani et al. [13–15].

$$\frac{1}{Pr}\frac{\partial u'}{\partial t}+Re\,\bar{u}\frac{\partial u'}{\partial x}+\frac{Re}{B^2}v'\frac{\partial \bar{u}}{\partial y}+Re\,w'\frac{\partial \bar{u}}{\partial z} = -\frac{\partial P'}{\partial x}+\nabla^2 u' \tag{12}$$

$$\frac{1}{Pr}\frac{\partial v'}{\partial t}+Re\,\bar{u}\frac{\partial v'}{\partial x} = -\frac{\partial P'}{\partial y}+\nabla^2 v' \tag{13}$$

$$\frac{1}{Pr}\frac{\partial w'}{\partial t}+Re\,\bar{u}\frac{\partial w'}{\partial x} = -\frac{\partial P'}{\partial z}+\nabla^2 w'+Ra\,T' \tag{14}$$

$$\frac{\partial T'}{\partial t}+Re\,Pr\,\bar{u}\frac{\partial T'}{\partial x}-w' = \nabla^2 T' \tag{15}$$

where $\nabla^2 = (\partial^2/\partial x^2)+(1/B^2)(\partial^2/\partial y^2)+(\partial^2/\partial z^2)$, $Re = \langle \bar{U} \rangle h/\nu^0$ is the Reynolds number, $Ra = g\beta^0(T_h - T_c)h^3/\nu^0\alpha^0$ is the Rayleigh number and $Pr = \nu^0/\alpha^0$ is the Prandtl number. Note that here we have used different scaling factors for the basic flow and for the disturbances, namely:

$$U' \to \frac{\alpha^0}{h}u' \quad T'-T^0 \to (T_h-T_c)T'$$

$$V' \to \frac{\alpha^0}{l}v' \quad P' \to \frac{\alpha^0\nu^0\rho^0}{h^2}P' \quad \bar{U} \to \langle \bar{U} \rangle \bar{u} \tag{16}$$

$$W' \to \frac{\alpha^0}{h}w' \quad t \to \frac{h^2}{\alpha^0}t$$

Assuming

$$\begin{pmatrix} u'(x,y,z,t) \\ v'(x,y,z,t) \\ w'(x,y,z,t) \\ P'(x,y,z,t) \\ T'(x,y,z,t) \end{pmatrix} = \begin{pmatrix} \hat{u}(y,z) \\ \hat{v}(y,z) \\ \hat{w}(y,z) \\ \hat{P}(y,z) \\ \hat{T}(y,z) \end{pmatrix} e^{ik_x x}\, e^{\sigma t} \tag{17}$$

where k_x is the wave number of the disturbance in the x-direction, and σ the amplification factor, we get:

$$ik_x\hat{u}+\frac{1}{B^2}\frac{\partial \hat{v}}{\partial y}+\frac{\partial \hat{w}}{\partial z}=0 \tag{18}$$

$$\frac{\sigma}{Pr}\hat{u}+ik_x\,Re\,\bar{u}\hat{u}+\frac{Re}{B^2}\frac{\partial \bar{u}}{\partial y}\hat{v}+Re\frac{\partial \bar{u}}{\partial z}\hat{w} = -ik_x\hat{P}+(\nabla_2^2-k_x^2)\hat{u} \tag{19}$$

$$\frac{\sigma}{Pr}\hat{v}+ik_x\,Re\,\bar{u}\hat{v} = -\frac{\partial \hat{P}}{\partial y}+(\nabla_2^2+k_x^2)\hat{v} \tag{20}$$

$$\frac{\sigma}{Pr}\hat{w} + ik_x\ Re\ \bar{u}\hat{w} = -\frac{\partial \hat{P}}{\partial z} + (\nabla_2^2 - k_x^2)\hat{w} + Ra\ \hat{T} \tag{21}$$

$$\sigma\hat{T} + ik_x\ Re\ Pr\ \bar{u}\hat{T} - \hat{w} = (\nabla_2^2 - k_x^2)\hat{T} \tag{22}$$

where $\nabla_2^2 = (1/B^2)(\partial^2/\partial y^2) + (\partial^2/\partial z^2)$ is the 2-D Laplace operator.

At this stage, two cases have to be considered: $k_x = 0$ and $k_x \neq 0$.

2.3. $k_x = 0$: the longitudinal rolls

Eqs. (18)–(22) reduce to:

$$\frac{1}{B^2}\frac{\partial \hat{v}}{\partial y} + \frac{\partial \hat{w}}{\partial z} = 0 \tag{23}$$

$$\frac{\sigma}{Pr}\hat{u} + \frac{Re}{B^2}\frac{\partial \bar{u}}{\partial y}\hat{v} + Re\frac{\partial \bar{u}}{\partial z}\hat{w} = \nabla_2^2\hat{u} \tag{24}$$

$$\frac{\sigma}{Pr}\hat{v} = -\frac{\partial \hat{P}}{\partial y} + \nabla_2^2\hat{v} \tag{25}$$

$$\frac{\sigma}{Pr}\hat{w} = -\frac{\partial \hat{P}}{\partial z} + \nabla_2^2\hat{w} + Ra\ \hat{T} \tag{26}$$

$$\sigma\hat{T} - \hat{w} = \nabla_2^2\hat{T} \tag{27}$$

Eqs. (23), (25)–(27) is the standard 2-D Rayleigh–Bénard eigenvalue problem for $\hat{v}$, $\hat{w}$, $\hat{P}$ and $\hat{T}$ (except for the lateral confinement given by B which does not allow a normal mode analysis in the y-direction) on which is based the calculation of $Ra^*_{//}$, independent of Re and Pr, already solved before in Ref. [34].

2.4. $k_x \neq 0$: computation of the 3-D structures by the Galerkin method

When $k_x \neq 0$, the system of five equations (18)–(22) can be reduce to three equations by eliminating $\hat{u}$ from Eq. (18) and $\hat{P}$ from Eq. (19). Eqs. (20)–(22) become:

$$\begin{aligned} &Q\hat{v} - \frac{1}{k_x^2 B^2}\frac{\partial}{\partial y}Q\frac{\partial \hat{v}}{\partial y} + \frac{i\ Re}{k_x B^2}\left(\frac{\partial^2 \bar{u}}{\partial y^2}\hat{v} + \frac{\partial \bar{u}}{\partial y}\frac{\partial \hat{v}}{\partial y}\right) \\ &\quad - \frac{1}{k_x^2}\frac{\partial}{\partial y}Q\frac{\partial \hat{w}}{\partial z} + \frac{i\ Re}{k_x}\left(\frac{\partial^2 \bar{u}}{\partial y\ \partial z}\hat{w} + \frac{\partial \bar{u}}{\partial z}\frac{\partial \hat{w}}{\partial y}\right) = 0 \end{aligned} \tag{28}$$

$$\begin{aligned} &Q\hat{w} - \frac{1}{k_x^2}\frac{\partial}{\partial z}Q\frac{\partial \hat{w}}{\partial z} + \frac{i\ Re}{k_x}\left(\frac{\partial^2 \bar{u}}{\partial z^2}\hat{w} + \frac{\partial \bar{u}}{\partial z}\frac{\partial \hat{w}}{\partial z}\right) \\ &\quad - \frac{1}{k_x^2 B^2}\frac{\partial}{\partial z}Q\frac{\partial \hat{v}}{\partial y} + \frac{i\ Re}{k_x B^2}\left(\frac{\partial^2 \bar{u}}{\partial y\ \partial z}\hat{v} + \frac{\partial \bar{u}}{\partial y}\frac{\partial \hat{v}}{\partial z}\right) \\ &\quad - Ra\ \hat{T} = 0 \end{aligned} \tag{29}$$

$$\sigma\hat{T} + ik_x\ Re\ Pr\ \bar{u}\hat{T} - (\nabla_2^2 - k_x^2)\hat{T} - \hat{w} = 0 \tag{30}$$

where the operator Q is defined by: $Q = \sigma/Pr + ik_x\ Re\ \bar{u} - (\nabla_2^2 - k_x^2)$. Note that $\partial/\partial y$ or $\partial/\partial z$ do not commute with Q.

The unknowns ($\hat{v}$, $\hat{w}$, $\hat{T}$) verify the following boundary conditions:

$$\hat{v}\left(y = \pm\frac{1}{2}\right) = \hat{v}\left(z = \pm\frac{1}{2}\right) = \frac{\partial \hat{v}}{\partial y}\left(y = \pm\frac{1}{2}\right) = 0 \tag{31}$$

$$\hat{w}\left(y = \pm\frac{1}{2}\right) = \hat{w}\left(z = \pm\frac{1}{2}\right) = \frac{\partial \hat{w}}{\partial z}\left(z = \pm\frac{1}{2}\right) = 0 \tag{32}$$

$$\hat{T}\left(z = \pm\frac{1}{2}\right) = \frac{\partial \hat{T}}{\partial y}\left(y = \pm\frac{1}{2}\right) = 0 \tag{33}$$

The third condition for $\hat{v}$ and $\hat{w}$ is deduced from the continuity equation (18) and the boundary conditions for $\hat{u}$: $\hat{u}(y = \pm 1/2) = \hat{u}(z = \pm 1/2) = 0$.

The system of three equations (28)–(30) together with the boundary conditions (31)–(33) is solved by the classical Galerkin technique:

$$\hat{v}(y, z) = \sum_{i=1}^{I\ \mathrm{MAX}} \sum_{j=1}^{J\ \mathrm{MAX}} a_{ij} \times A_i(y)B_j(z) \tag{34}$$

$$\hat{w}(y, z) = \sum_{k=1}^{K\ \mathrm{MAX}} \sum_{l=1}^{L\ \mathrm{MAX}} b_{kl} \times C_k(y)D_l(z) \tag{35}$$

$$\hat{T}(y, z) = \sum_{m=1}^{M\ \mathrm{MAX}} \sum_{n=1}^{N\ \mathrm{MAX}} c_{mn} \times E_m(y)F_n(z) \tag{36}$$

where $(A_i(y))_{i=1,I\ \mathrm{MAX}}$, $(B_j(z))_{j=1,J\ \mathrm{MAX}}$, …, $(F_n(z))_{n=1,N\ \mathrm{MAX}}$ are six complete sets of linearly independent trial functions verifying the boundary conditions of the problem. The computation of the coefficients a_{ij}, b_{kl} and c_{mn} is carried out by the method of weighted residues and yields an algebraic system of linear equations or, equivalently, the following eigenvalue problem (noted $\mathscr{L}$):

$$\mathscr{L} \Leftrightarrow (\overline{\overline{M}} + i\,Re\,\overline{\overline{P}} - \sigma\overline{\overline{N}})\begin{pmatrix}\mathbf{a}\\ \mathbf{b}\\ \mathbf{c}\end{pmatrix} = 0 \tag{37}$$

where $\overline{\overline{M}}$, $\overline{\overline{N}}$ and $\overline{\overline{P}}$ are square matrices of size $S = (I \quad \mathrm{MAX}\times J \quad \mathrm{MAX}+K \quad \mathrm{MAX}\times L \quad \mathrm{MAX}+M \quad \mathrm{MAX}\times N \quad \mathrm{MAX})^2$, and **a**, **b** and **c** are the vectors constructed with (a_{ij}), (b_{kl}) and (c_{mn}), respectively. Next, we search for the complex eigenvalues σ of the matrix $(\overline{\overline{N}}^{-1}\overline{\overline{M}} + i\,Re\,\overline{\overline{N}}^{-1}\overline{\overline{P}})$ and the corresponding eigenvectors (**a**, **b**, **c**), from which we get the disturbances ($\hat{v}$, $\hat{w}$, $\hat{T}$). In fact, we are only interested in the highest real part $\sigma_r^{\max}$ (the most destabilising disturbance), and in the corresponding eigenvector. The associated imaginary part represents the time pulsation of the perturbations. The linear instability threshold is given by $\sigma_r^{\max} = 0$. The critical Rayleigh number Ra^* and wave number k_x^* correspond to the minimum of the curve $Ra = f(k_x)$ obtained when $\sigma_r^{\max} = 0$; $\sigma_i^* = \sigma_i(Ra^*, k_x^*)$ is the critical time pulsation. The Fortran subroutines used in order to find the eigenvalues have been extracted from the Eispack package [35], and adapted in double precision.

2.5. Taking into account the evenness of the solutions

In (34)–(36), we do not know a priori if the trial functions are even or odd functions of y and z. Therefore, we split each variable into the sum of four terms of different evenness:

$$\begin{cases}\hat{v}(y,z) = \hat{v}^{EE}(y,z) + \hat{v}^{EO}(y,z) + \hat{v}^{OE}(y,z) + \hat{v}^{OO}(y,z)\\ \hat{w}(y,z) = \hat{w}^{EE}(y,z) + \hat{w}^{EO}(y,z) + \hat{w}^{OE}(y,z) + \hat{w}^{OO}(y,z)\\ \hat{T}(y,z) = \hat{T}^{EE}(y,z) + \hat{T}^{EO}(y,z) + \hat{T}^{EO}(y,z) + \hat{T}^{OO}(y,z)\end{cases} \tag{38}$$

where the superscripts 'E' stands for 'even' and 'O' for 'odd', the first subscript relating to y and the second to z. Then, each of the four terms of the relations (38) is developed in a series of trial functions of prescribed evenness. For instance:

$$\hat{v}^{EO}(y,z) = \sum_{i=1}^{I\,\mathrm{MAX}}\sum_{j=1}^{J\,\mathrm{MAX}} a_{ij}^{EO} \times A_i^E(y) B_j^O(z) \tag{39}$$

where A_i^E is even in y and B_j^O is odd in z.

In this study, we have chosen the following trial functions which all satisfy the boundary conditions (31)–(33):

$$\begin{cases}A_i^E(y) = (y^2 - \frac{1}{4})^2 T_{2i-2}(y); \quad A_i^O(y) = (y^2 - \frac{1}{4})^2 T_{2i-1}(y)\\ B_j^E(z) = (z^2 - \frac{1}{4}) T_{2j-2}(z); \quad B_j^O(z) = (z^2 - \frac{1}{4}) T_{2j-1}(z)\\ C_k^E(y) = (y^2 - \frac{1}{4}) T_{2k-2}(y); \quad C_k^O(y) = (y^2 - \frac{1}{4}) T_{2k-1}(y)\\ D_l^E(z) = (z^2 - \frac{1}{4})^2 T_{2l-2}(z); \quad D_l^O(z) = (z^2 - \frac{1}{4})^2 T_{2l-1}(z)\\ E_m^E(y) = (-1)^m \cos[(2m-2)\pi y]; \quad E_m^O(y) = (-1)^{m+1} \sin[(2m-1)\pi y]\\ F_n^E(z) = (z^2 - \frac{1}{4}) T_{2n-2}(z); \quad F_n^O(z) = (z^2 - \frac{1}{4}) T_{2n-1}(z)\end{cases} \tag{40}$$

where the $T_n(x)$ are the Chebyshev polynomials defined by: $T_n(x) = \cos(n \arccos(x)) = 2xT_{n-1}(x) - T_{n-2}(x)$.

The eigenvalue problem $\mathscr{L}$ defined by (37) splits up into the sum of four distinct eigenvalue problems $\mathscr{L}_A$, $\mathscr{L}_B$, $\mathscr{L}_C$ and $\mathscr{L}_D$:

$$\begin{array}{ccccccccc}\mathscr{L} & = & \mathscr{L}_A & + & \mathscr{L}_B & + & \mathscr{L}_C & + & \mathscr{L}_D\\ \downarrow & & \downarrow & & \downarrow & & \downarrow & & \downarrow\\ \begin{pmatrix}\hat{v}\\ \hat{w}\\ \hat{T}\end{pmatrix} & & \begin{pmatrix}\hat{v}^{OO}\\ \hat{w}^{EE}\\ \hat{T}^{EE}\end{pmatrix} & & \begin{pmatrix}\hat{v}^{EO}\\ \hat{w}^{OE}\\ \hat{T}^{OE}\end{pmatrix} & & \begin{pmatrix}\hat{v}^{EE}\\ \hat{w}^{OO}\\ \hat{T}^{OO}\end{pmatrix} & & \begin{pmatrix}\hat{v}^{OE}\\ \hat{w}^{EO}\\ \hat{T}^{EO}\end{pmatrix}\end{array} \tag{41}$$

Indeed, for homogeneity reasons, any association is not allowed. As an example, suppose that we select a disturbance $\hat{u}$ which is odd in y and odd in z, $\hat{u} = \hat{u}^{OO}$. From the continuity equation (18), $\hat{v}$ must be even in y, but remains odd in z, $\hat{v} = \hat{v}^{EO}$; similarly, $\hat{w} = \hat{w}^{OE}$ and, from the energy equation (22), $\hat{T}$ must have the same evenness as $\hat{w}$, i.e. $\hat{T} = \hat{T}^{OE}$.

The evenness of the four possible cases is given in Table 3, where we have also drawn different possible roll patterns in the (y, z) plane, from the components $\hat{v}$ and $\hat{w}$ of the velocity perturbations. To get the complete structures, the spatial evolution of $\hat{u}$ and the x-dependence of the perturbations (of the form $e^{ik_x x}$) must be taken into account. In the limiting case

Table 3
Possible forms of the perturbations in the (y, z) plane deduced from the y and z evenness of their amplitudes

	Case A		Case B		Case C		Case D	
	y	z	y	z	y	z	y	z
u'	E	O	O	O	O	E	E	E
v'	O	O	E	O	E	E	O	E
w'	E	E	O	E	O	O	E	O
T'	E	E	O	E	O	O	E	O
P'	E	O	O	O	O	E	E	E
	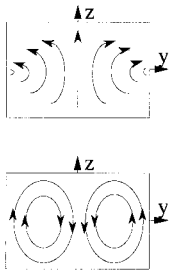		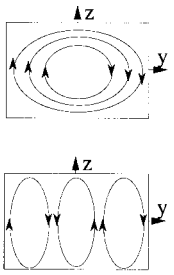		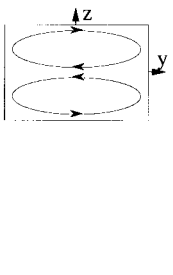		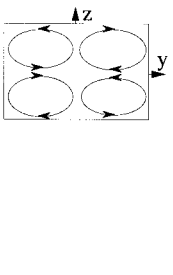	
	- even number of $R_{//}$ when $k_x \to 0$; - horseshoe-shaped $R_\perp$ when $k_x \approx 3$.		- odd number of $R_{//}$ when $k_x \to 0$; - physically never observed patterns when $k_x > 0$.		- physically never observed patterns whatever k_x.		- physically never observed patterns whatever k_x.	

$k_x \to 0$, the form of the convective rolls can be directly deduced from what is sketched in the (y, z) plane in Table 3. Different types of $R_{//}$ are liable to appear: an even number of $R_{//}$ in Case A, an odd number of $R_{//}$ in Case B, and an even number of superposed $R_{//}$ in Cases C and D. We have verified that the critical Rayleigh number obtained from the eigenvalue problems $\mathscr{L}_C$ and $\mathscr{L}_D$ are always clearly higher than for the Cases A and B.

When $k_x > 0$, complex 3-D structures are observed since the y-velocity component never vanishes (cf. [23] and Fig. VI-34 of this reference). In Case A, the computations show that the critical Rayleigh number is reached for $k_x \approx 3$, and that the thermoconvective structures appear like horseshoe-shaped transversal rolls, as if the $R_\perp$ were bent by the adherence effects on the lateral walls. In Fig. 5, the form of the $R_\perp$ at the critical point is shown from the isotherms of T', deduced from the eigenvectors of problem $\mathscr{L}_A$. The isocontours of T' are drawn in the planes $x = 0$, $y = 0$ and $z = 0$, for a flow at $Pr = 10$ in a duct of aspect ratio $B = 5$, and for $Re = 0$, 0.4 and 1.2. The drawings in plane $z = 0$ (top view) clearly show that the rolls are more and more bent as Re increases. Although the axis of these rolls is not a straight line, we will continue noting them by $R_\perp$. When $k_x > 0$, for

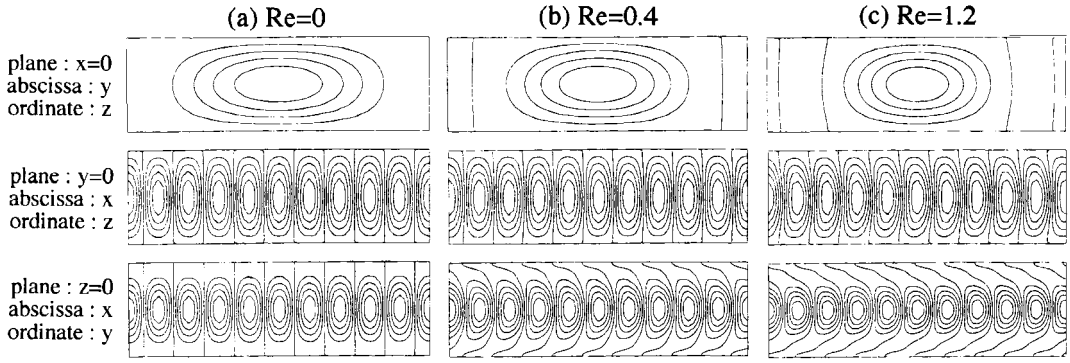

Fig. 5. Isocontours of T' at the critical point, in the planes $x = 0$, $y = 0$ and $z = 0$, for a flow at $Pr = 10$, in a duct of aspect ratio $B = 5$, and for $Re = 0$, 0.4 and 1.2.

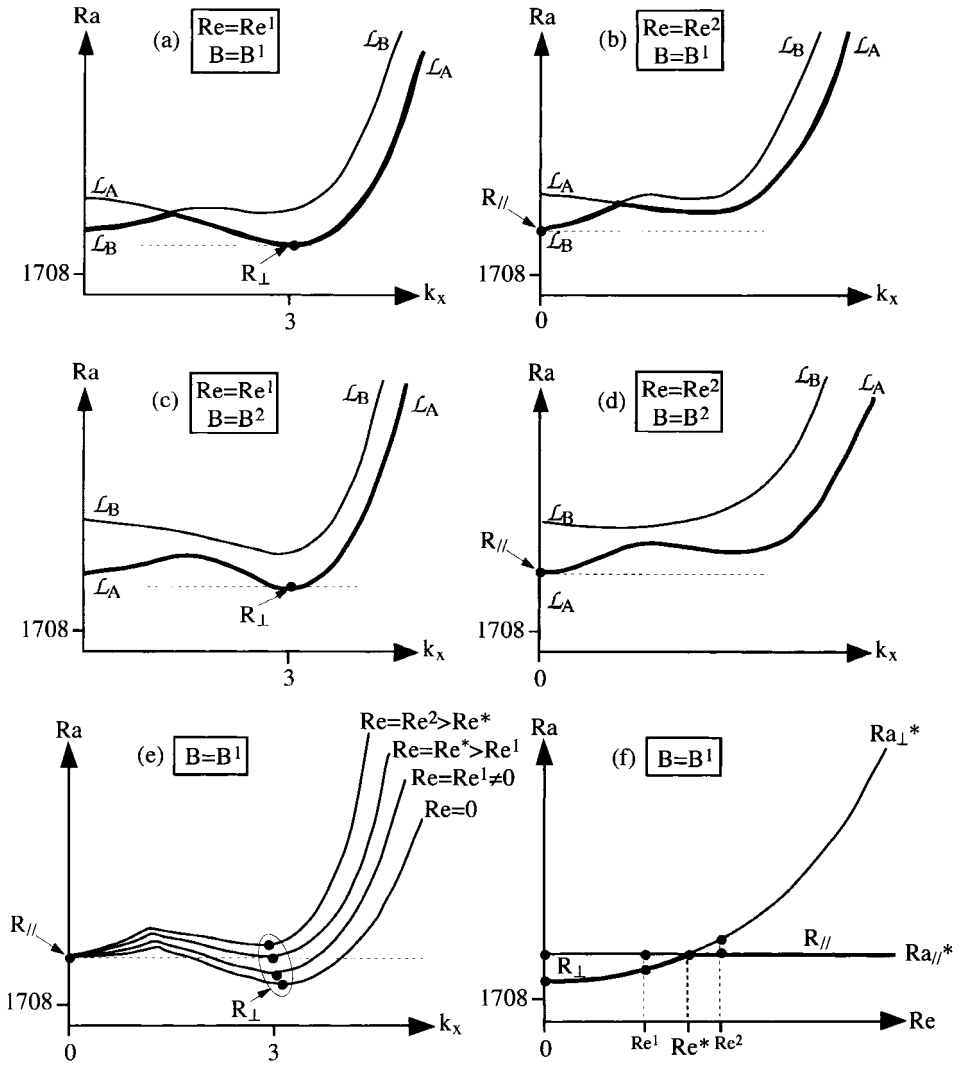

Fig. 6. The different steps to get the critical Reynolds number Re^*, for a duct of given aspect ratio B, and for Pr = cst.

Case B in Table 3, the corresponding flow pattern has never been experimentally observed. Indeed, the amplitude of u' vanishes in the median vertical plane $y = 0$ because u' is odd with respect to y.

2.6. Computation of the critical parameters of the flow

The two eigenvalue problems which have to be solved ($\mathscr{L}_A$ and $\mathscr{L}_B$) involve six parameters: k_x, σ, Ra, Re, Pr and B. Fig. 6 explains the different steps to get the critical Reynolds number Re^* at a given Prandtl number Pr and at a given aspect ratio B. As already said, the first step consists in seeking the minimum value of Ra when k_x varies between 0 and $+\infty$, for $\sigma_r^{\max} = 0$. In graphs 6(a) and (b), for $B = B^1$ close to an odd number, as an example, the bold point indicates the position of the critical point (k_x^*, Ra^*). Fig. 6(a) shows the case of a flow at small Reynolds number $Re = Re^1$, for which the minimum value of Ra is obtained at $k_x \approx 3$ by solving the eigenvalue problem $\mathscr{L}_A$. Therefore, when $Re = Re^1$, the thermoconvective patterns at the instability threshold take the form of 3-D horseshoe-shaped transversal rolls. Fig. 6(b) shows the case of a flow at $Re = Re^2 > Re^1$, for which the critical Rayleigh number is obtained at $k_x = 0$ by solving an eigenvalue problem of type $\mathscr{L}_B$. Therefore, the thermoconvective patterns at the instability threshold correspond to an odd number of longitudinal rolls. If we take $B = B^2$, close to an even number, then the situation is sketched in Figs. 6(c) and 6(d), such that the eigenvalue problem $\mathscr{L}_A$ always provides Ra^*. Four neutral stability curves $Ra = f(k_x)$ at different Reynolds

Table 4
$Ra^*_{//}$ as a function of B, with indication of the number of $R_{//}$ and of the type of the eigenvalue problem giving the critical values

Transversal aspect ratio B	Critical Rayleigh number $Ra^*_{//}$	Type of the eigenvalue problem ($\mathscr{L}_A$ or $\mathscr{L}_B$)	Number of $R_{//}$
0.1	5,082,050	$\mathscr{L}_B$	1
0.5	12,113.3	$\mathscr{L}_B$	1
1	2585.03	$\mathscr{L}_B$	1
2	2013.24	$\mathscr{L}_A$	2
3	1870.72	$\mathscr{L}_B$	3
3.64	1848.87	$\mathscr{L}_B$	3
4	1810.48	$\mathscr{L}_A$	4
5	1779.00	$\mathscr{L}_B$	5
5.4	1767.28	$\mathscr{L}_B$	5
∞	*1707.76*	$\mathscr{L}_A$ or $\mathscr{L}_B$	∞

numbers, including Re^1 and Re^2, are given in graph 6(e) for the case $B=B^1$. It can be seen that the critical point at $k_x=0$ ($Ra^*_{//}$) is not affected by the flow rate. On the other hand, the flow rate has a stabilizing effect on the $R_\perp$ at $k_x \approx 3$. The critical Reynolds number Re^* corresponds to a neutral stability curve $Ra=f(k_x)$ with two equal minima: the first at $k_x=0$ and the second at $k_x \approx 3$. For $Re < Re^*$, the smallest Rayleigh numbers correspond to the appearance of the $R_\perp$, while for $Re > Re^*$, the smallest Rayleigh number corresponds to the appearance of an even or odd number of $R_{//}$, depending on B. The neutral stability curves $Ra^*_\perp$ and $Ra^*_{//}$ obtained from Fig. 6(e) are shown on Fig. 6(f).

3. Results

3.1. A few results concerning the longitudinal rolls ($k_x=0$)

A few results, already published in [34], but which are important for what follows, are reported in Table 4 and Fig. 7. They concern the variation of the critical Rayleigh number for the longitudinal rolls $Ra^*_{//}$ with the transversal aspect ratio B.

Note that all these results are valid whatever Re and Pr.

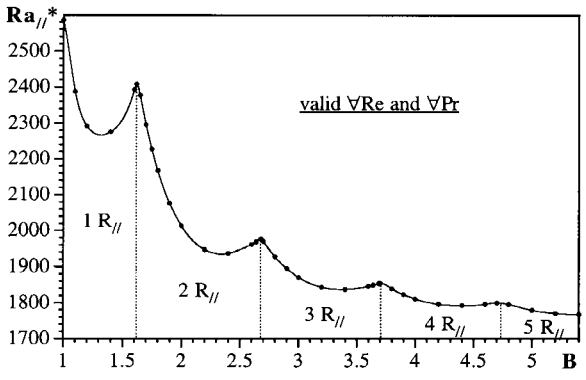

Fig. 7. Critical Rayleigh number for the longitudinal rolls as a function of the transversal aspect ratio, with indication of the number of $R_{//}$.

3.2. Critical parameters for the 2-D transversal rolls when $B \to \infty$

Critical values of $Ra^*_\perp$ when $B \to \infty$ provide a lower bound when B is finite and are thus interesting to know. The evolution of $Ra^*_\perp$ as a function of Re when $B \to \infty$ is shown in Fig. 8, for $Pr = 10^{-6}$, 1, 7, 10 and 453 (this last value corresponds to a particular silicon oil in some experiments reported in [9], while the first value should reflect the 'zero Prandtl number solution' expected to be valid for liquid metals). Well-known results are again found: $Ra^*_\perp$ increases when Re increases, and the basic flow is more stabilized when Pr is high. The numerical values of $Ra^*_\perp$ and k^*_x when $B \to \infty$ are given in Appendix A (Table A1).

Whatever the value of B, it may be shown that the principle of exchange of stability, i.e. $\sigma^*_i=0$, is only

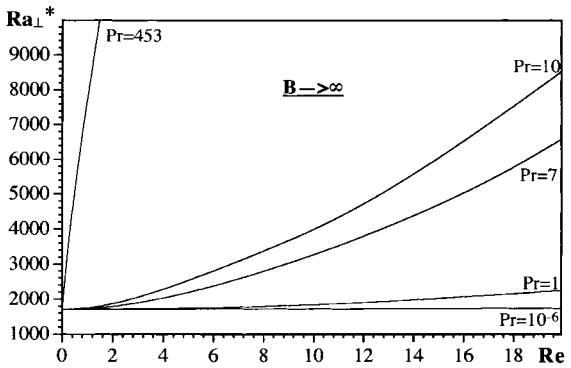

Fig. 8. Critical Rayleigh number for the transversal rolls as a function of Re when $B \to \infty$, at $Pr = 10^{-6}$, 1, 7, 10 and 453.

Table 5
Ratio of the $R_\perp$ velocity, Vr, to the average velocity of the 2-D basic flow ($\langle\bar{U}\rangle = U^0$), at the instability threshold, as a function of Re and Pr, when $B \to \infty$

Re	$(Vr/\langle\bar{U}\rangle)^*$ at $Pr = 10^{-6}$	$(Vr/\langle\bar{U}\rangle)^*$ at $Pr = 1$	$(Vr/\langle\bar{U}\rangle)^*$ at $Pr = 10$	$(Vr/\langle\bar{U}\rangle)^*$ at $Pr = 453$
0.2	0.8833	1.1703	1.296	1.380
0.4	0.8833	1.1703	1.296	1.410
0.6	0.8833	1.1703	1.296	1.424
0.8	0.8833	1.1703	1.297	1.432
1	0.8833	1.1703	1.297	1.438
2	0.8833	1.1703	1.300	1.453
3	0.8833	1.1702	1.304	1.459
4	0.8832	1.1701	1.309	1.462
6	0.8830	1.1700	1.320	1.465
8	0.8829	1.1696	1.329	1.465
10	0.8826	1.1692	1.335	1.463

satisfied when $Re = 0$. For infinite, as well as for finite transversal aspect ratios, we get oscillations ($\sigma_i^* \neq 0$) as soon as $Re \neq 0$. Thus, in the general case, at the linear instability threshold, the form of the perturbations corresponding to the $R_\perp$ is:

$$\begin{pmatrix} u'(x,\,y,\,z,\,t) \\ v'(x,\,y,\,z,\,t) \\ w'(x,\,y,\,z,\,t) \\ P'(x,\,y,\,z,\,t) \\ T'(x,\,y,\,z,\,t) \end{pmatrix} = \begin{pmatrix} \hat{u}(y,\,z) \\ \hat{v}(y,\,z) \\ \hat{w}(y,\,z) \\ \hat{P}(y,\,z) \\ \hat{T}(y,\,z) \end{pmatrix} e^{ik_x^* x}\, e^{i\sigma_i^* t} \tag{42}$$

Therefore, the $R_\perp$ behave like travelling waves of dimensionless critical wavelength $\lambda^* = 2\pi/k_x^*$, of dimensionless critical period $\tau^* = 2\pi/|\sigma_i^*|$, and of dimensionless critical velocity λ^*/τ^*. Remembering the scaling factors for length and time [cf. relations (3) and (16)], the dimensional wave velocity of the $R_\perp$ is $Vr^* = \lambda^* h/(\tau^* h^2/\alpha^0)$. We then define the ratio $(Vr/\langle\bar{U}\rangle)^*$ of the transversal roll velocity to the average velocity of the flow $\langle\bar{U}\rangle$ (cf. Table 2):

$$\left(\frac{Vr}{\langle\bar{U}\rangle}\right)^* = \frac{|\,\sigma_i^*(Re,\,Pr)\,|}{k_x^*(Re,\,Pr)}\,\frac{\alpha^0}{h}\,\frac{h}{Re\,\nu^0} = \frac{|\,\sigma_i^*(Re,\,Pr)\,|}{k_x^*(Re,\,Pr)}\,\frac{1}{Re\,Pr} \tag{43}$$

The ratio $(Vr/\langle\bar{U}\rangle)^*$ when $B \to \infty$ is given in Table 5 for $Pr = 10^{-6}$, 1, 10 and 453. $(Vr/\langle\bar{U}\rangle)^*$ varies with Re and Pr. However, this ratio can be considered almost as a constant, at a given Prandtl number, since the frequency of the wave σ_i^* is at first-order proportional to Re. Corrections in $O(Re^3)$ must be added at large Re [16]. Generally, $(Vr/\langle\bar{U}\rangle)^*$ is greater than unity (e.g. ~30% higher at $Pr = 10$), except when Pr is very small (e.g. $Pr = 10^{-6}$).

3.3. Critical parameters for the 3-D transversal rolls ($k_x^* \approx 3$)

Now, we focus on the variations of the critical parameters and of the critical characteristics [$Ra_\perp^*$, k_x^*, σ_i^* and $(Vr/\langle\bar{U}\rangle)^*$] of the 3-D $R_\perp$ flows, as a function of Re, B and Pr, respectively. All the results are presented in the form of figures, whereas the numerical data are given in Appendix B.

The evolution of $Ra_\perp^*$ as a function of Re is presented at $Pr = 10$, for $B = 1$, 2 and 5 in Fig. 9 (the case $B \to \infty$ is also drawn on the figure). It can be noted that the stabilizing influence of the lateral vertical walls on the onset of the 3-D $R_\perp$ is more pronounced in narrow ducts. The dotted horizontal lines are from Table 4. Thus, the values of Re^* at $Pr = 10$ can be determined from Fig. 9: $Re^* \approx 0.6$, 1.2 and 1.1 for $B = 1$, 2 and 5, respectively [cf. Table B1 in Appendix B for the precise values and Fig. 10 for $Re^* = f(B)$]. Note that the variation of Re^* with B is

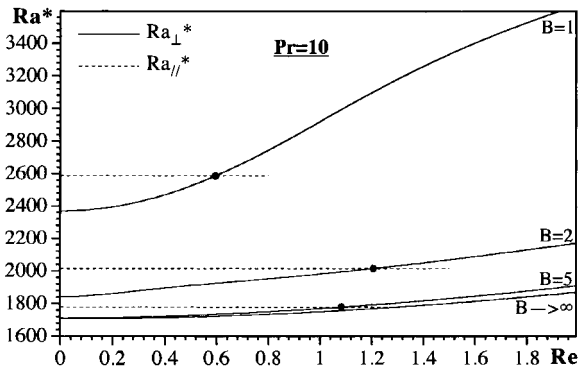

Fig. 9. Critical Rayleigh number $Ra_\perp^*$ for the 3-D $R_\perp$, as a function of Re, at $Pr = 10$, for different aspect ratios B of the duct; the intersection with the horizontal lines $Ra_{//}^* = f(Re)$ is also drawn; $S = 48 \times 48$.

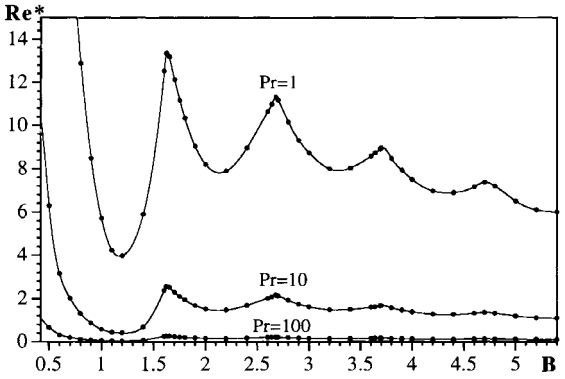

Fig. 10. Critical Reynolds number Re^* as a function of the aspect ratio of the duct B, for $Pr = 1, 10, 100$; $S = 12 \times 12$.

not monotonous. In the limit case $B \to \infty$, convection always appears in the form of $R_{//}$ and $Re^* = 0$. On the other hand, when $B \to 0$ and when there is no average flow ($Re = 0$), it can be shown from [36,37] that $Ra^*_{\perp}$ and $Ra^*_{//}$ tends to infinity according to the following laws:

$$\text{when } B \to 0, \quad \begin{cases} Ra^*_{\perp}(Re=0) \to \dfrac{\text{cst}}{B^2} & [36] \\ Ra^*_{//}(Re=0) \to \dfrac{500.56}{B^4} & [37] \end{cases} \tag{44}$$

Thus, the difference $(Ra^*_{//} - Ra^*_{\perp})(Re = 0)$, which partly determines Re^*, tends to infinity when $B \to 0$. Therefore, when the transversal aspect ratio B of a duct is very small, Re^* is very high and the convection is expected to appear in the form of transversal rolls.

The variation of k^*_x as a function of Re is plotted on Fig. 11, at $Pr = 10$ and $B = 1$, 2, 5 and ∞. The critical wave number is shown to decrease monotonously when Re increases (except at $B = 1$). Note the significative influence of Re on k^*_x particularly at $B = 2$. The variation of $(Vr/\langle \bar{U} \rangle)^*$ as a function of Re, as well as the variation of $(Vr/\bar{U}^{\max})^*$ (cf. Table 2), are presented in Fig. 12, at $Pr = 10$ and $B = 1$, 2, 5 and ∞. It can be noted that these two ratios are almost independent of Re as already said in the discussion of Eq. (43). Whatever B, the propagation velocity of the 3-D $R_{\perp}$ is higher than the average velocity of the basic flow (except at $Pr = 10^{-6}$, cf. Table 5), but slower than the maximum velocity, according to the relation between $\langle \bar{U} \rangle$ and $\bar{U}^{\max}$ of Table 2.

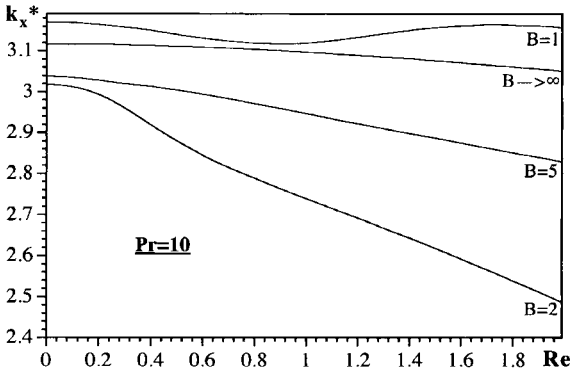

Fig. 11. Critical wave number k^*_x for the 3-D $R_{\perp}$, as a function of Re, for $B = 1$, 2, 5 and $B \to \infty$, at $Pr = 10$; $S = 48 \times 48$.

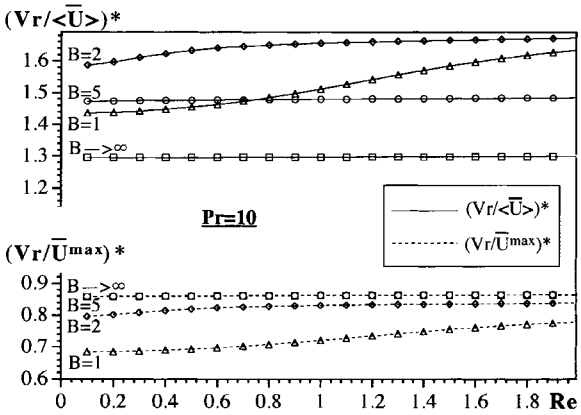

Fig. 12. Ratios of the wave velocity Vr of the 3-D $R_{\perp}$ at the critical point to the average velocity $\langle \bar{U} \rangle$ or to the maximum velocity $\bar{U}^{\max}$ of the basic flow, as a function of Re, for $B = 1$, 2, 5 and $B \to \infty$, at $Pr = 10$; $S = 48 \times 48$.

Fig. 10 gives the critical Reynolds numbers Re^* as a function of the aspect ratio, for $Pr = 1$, 10 and 100 (see also Table B3 in Appendix B for $Pr = 453$). As said before, Re^* tends to infinity when $B \to 0$, and tends to zero when $B \to \infty$. The three curves present a series of minima and maxima which coincide with the minima and maxima of the curves $Ra^*_{//} = f(B)$ of Fig. 7, a fact that can be easily understood as follows: each time that there is a maximum in Fig. 7, that means that $R_{//}$ are difficult to form or, in other words, that the Reynolds number necessary to align the rolls parallel to the mean flow must be high. The effect of Pr can also be explained: small Pr means small viscosity, thus higher Reynolds numbers. Note that, for usual liquids (say water, $Pr = 7$), the transitional Reynolds number remains of order 1: $Re^* > 15$ is only attained when $B < 1$ and $Pr < 1$.

The critical wave number k^*_x of the 3-D $R_{\perp}$ when $Re = Re^*(B, Pr)$ is given as a function of B for $Pr = 1$, 10, 100 and 453 in Fig. 13. k^*_x tends to 3.116 when $B \to \infty$. Note that k^*_x practically does not change with Pr, for $Pr > 1$ and $B > 1$. The variation of $(Vr/\langle \bar{U} \rangle)^*$ as a function of B, when $Re = Re^*$, is presented on Fig. 14. From Figs. 13 and 14, it appears that the variations of $k^*_x(Re^*)$ and $(Vr/\langle \bar{U} \rangle)^*(Re^*)$ with B are more regular when $B > 1.6$ than when B is smaller.

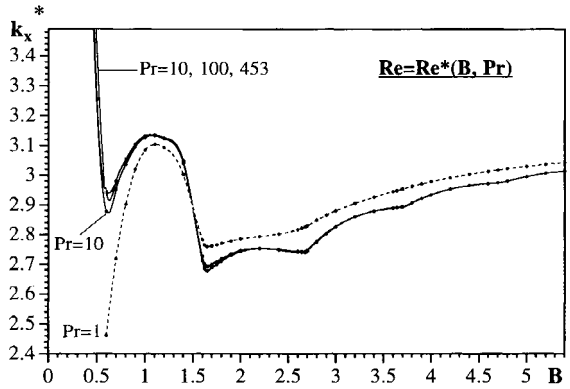

Fig. 13. Critical wave number k_x^* at $Re = Re^*$, as a function of the aspect ratio of the duct B, for Pr = 1, 10, 100 and 453; $S = 12 \times 12$.

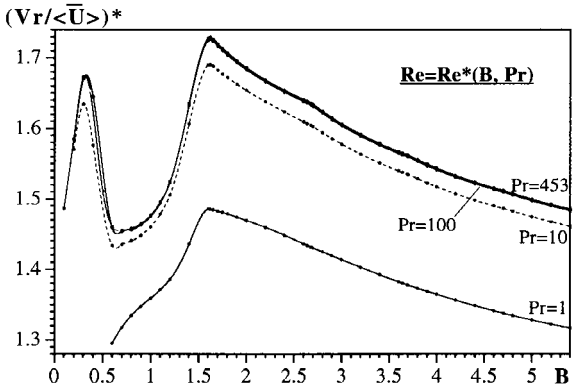

Fig. 14. $(Vr/\langle\bar{U}\rangle)^*$ as a function of B, at $Re = Re^*(B, Pr)$ and for different Prandtl numbers; $S = 12 \times 12$.

The numerical values of the critical parameters when $Re = Re^*$ are listed as a function of Pr, for B = 2 and 5.2, in Table B4 of Appendix B. From this table, we successively present the functions $\mathrm{Log}(Re^*) = f(\mathrm{Log}(Pr))$, $k_x^* = f(\mathrm{Log}(Pr))$ and $(Vr/\langle\bar{U}\rangle)^* = f(\mathrm{Log}(Pr))$, for B = 5.2, in Figs. 15–17. From Fig. 15, it appears that, when Pr is sufficiently small ($Pr < 0.01$ when B = 5.2), Re^* tends to a constant (which in fact depends on the aspect ratio). That means that, even at Pr = 0, $Ra_\perp^*$ still increases when Re increases. On the other hand, for 'high' values of Pr ($Pr > 5$ when B = 5.2), Re^* tends to zero following a law of the type; $Re^* = C(B)/Pr$, where $C(B)$ is a function of B. In Fig. 16, it can be noted that the wave number k_x^* at the critical point $Re = Re^*$ tends to a constant when Pr is small ($Pr < 0.01$). From the ratio $(Vr/\langle\bar{U}\rangle)^*$ at the critical point $Re = Re^*$ and for B = 5.2 (cf. Fig. 17), the wave travels at the mean velocity at small Pr ($Pr < 0.01$, say liquid metals), but at 1.4 to 1.5 times

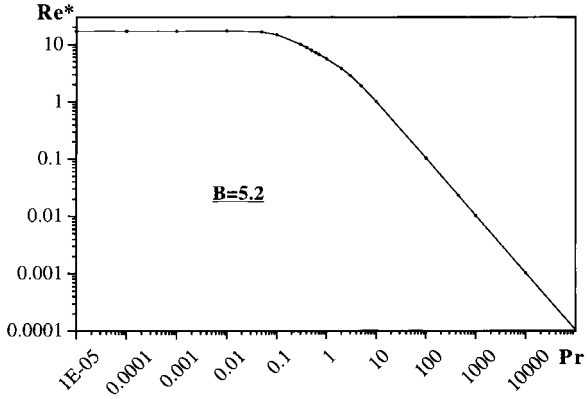

Fig. 15. Re^* as a function of Pr, at B = 5.2; $S = 48 \times 48$.

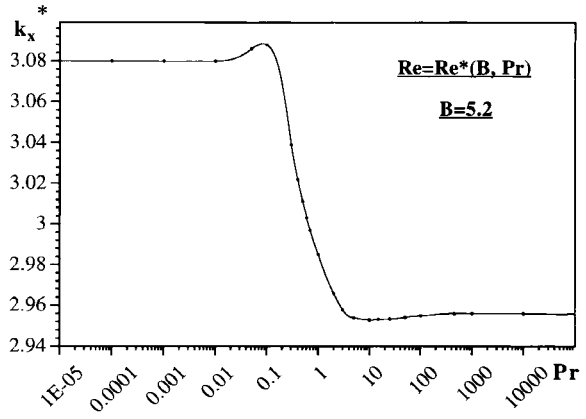

Fig. 16. k_x^* as a function of Pr, at $Re = Re^*(B, Pr)$ and B = 5.2; $S = 48 \times 48$.

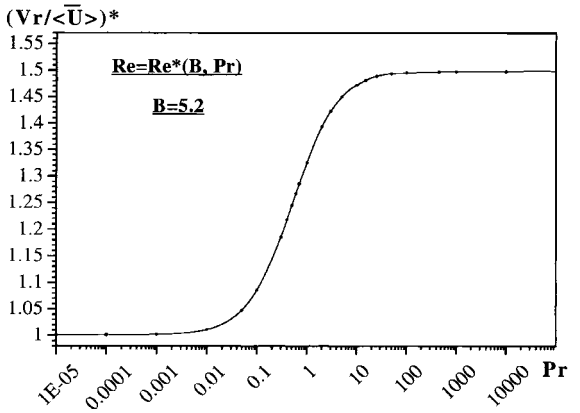

Fig. 17. $(Vr/\langle\bar{U}\rangle)^*$ as a function of Pr, at $Re = Re^*(B, Pr)$ and B = 5.2; $S = 48 \times 48$.

Table 6
Comparison of experimental or numerical values of $Ra^*_{//}$ and Re^* found in the literature with the values obtained by the present linear stability study

Reference	Methodology	Pr	B	$Ra^*_{//}$	Re^*
Chen and Lavine [40]	3-D numerical simulation	0.7	2	2000	5 ± 1
Present study	Linear stability			2013	8.5
Ouazzani et al. [13,14]	LDA	6.4	3.6	1840 ± 80	0.35 ± 0.1
Present study	Linear stability			1849	1.7
Luijkx et al. [24]	Shadowgraphy	453	5.25	1710 ± 220	$(6.4 \pm 0.8) \times 10^{-3}$
Present study	Linear stability			1770	23×10^{-3}

the mean velocity for all organic liquids (the smallest Prandtl number for a transparent liquid is found to be equal to 4 for acetone).

4. Discussion and conclusions

4.1. About the critical Rayleigh and Reynolds numbers: $Ra^*_{//}$, $Ra^*_{\perp}$ and Re^*

In Table 6, we present values of $Ra^*_{//}$ and Re^* obtained experimentally or by 3-D direct numerical simulations in three different papers, at different Prandtl numbers and aspect ratios. These values are compared with those obtained by the present 3-D linear stability study. It can be noted that the values of $Ra^*_{//}$ are in excellent agreement. However, the values of Re^* computed by the linear theory give only an upper bound. This is quite natural since the notions of convective instability, which introduces a new critical Rayleigh number curve (noted $Ra^{conv}_{\perp}$), has to be invoked. For $Ra^*_{\perp} < Ra < Ra^{conv}_{\perp}$, the flow is convectively unstable: the basic flow remains stable if it is submitted to a *unique* perturbation that grows in time, but that is carried out of the duct by the mean flow; however, the basic flow becomes unstable when it is submitted to a permanent white noise (for instance). For $Ra > Ra^{conv}_{\perp}$, the flow is absolutely unstable: a unique perturbation is sufficient to produce a periodic pattern (see Refs. [38,39] for more details about the notions of convective and absolute instability).

In Fig. 18, we present the stability diagram of the PBF obtained experimentally by Ouazzani et al. [13,14], in the case of water ($Pr = 6.4$) in a 3.6-aspect ratio duct. This diagram is compared with the theoretical transition curves $Ra^*_{//}$ and $Ra^*_{\perp}$ computed for the experimental conditions $Pr = 6.4$ and $B = 3.6$, and also with the curve $Ra^{conv}_{\perp}$ only available from a Ginzburg–Landau approach for $B \to \infty$ [16,27]. The experimental stability diagram presents three main zones: the classical Poiseuille flow in Zone, I, transversal rolls in II, and longitudinal rolls in III.

As already seen in Table 6, the linear stability curve $Ra^*_{//}$ is in very good agreement with the horizontal separation line between Zones I and III. On the other hand, the curve $Ra^*_{\perp}$ does not correspond to the transition between Zones I and II and gives $Re^* \approx 1.7$, which is different from the experimental critical Reynolds number $Re^*_{exp} \approx 0.35$. Once again, this is quite natural since, in Ouazzani's experiments [13,14], no sustained mechanical perturbations are introduced

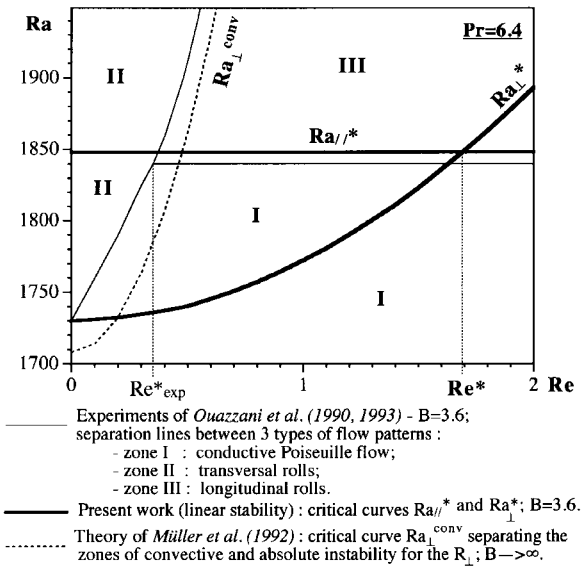

Fig. 18. Comparison of the stability diagram determined experimentally by Ouazzani et al. [13,14], with the results of the present linear stability study and with the weakly non-linear theory of Müller et al. [16] (see also [15]).

Table 7
Comparison of different values of $(Vr/\langle\tilde{U}\rangle)^*$ at $Re = Re^*$ found in the literature with the values obtained by the present linear stability study

Reference	$Vr/\langle\tilde{U}\rangle = f(Ra)$	Methodology	Pr	B	$(Vr/\langle\tilde{U}\rangle)^*$ at $Ra = Ra^*_{//}$
Schröder and Bülher [28]	$Vr/\langle\tilde{U}\rangle = 1.53–3.18 \times 10^{-5} Ra$	3-D numerical simulation	530	4.1	1.47
Present study		Linear stability			1.54
Ouazzani et al. [13]	$Vr/\langle\tilde{U}\rangle = 1.62–8.67 \times 10^{-5} Ra$	LDA	6.4	3.6	1.46
Present study		Linear stability			1.5
Nicolas et al. [33]	$Vr/\langle\tilde{U}\rangle = 1.28–0.82 \times 10^{-5} Ra$	2-D numerical simulation	6.4	∞	1.27
Present study		Linear stability			1.28
Müller et al. [16]	$Vr/\langle\tilde{U}\rangle = 1.19–1.1 \times 10^{-5} Ra$	Ginzburg–Landau equation	1	∞	1.17
Present study		Linear stability			1.17

near the inlet, and therefore, the curve $Ra_{\perp}^{\mathrm{conv}}$ agrees much better with the transition between Zones I and II. Thus, the weakly non-linear theory gives a critical Reynolds number $Re^* \approx 0.45$ much closer to the experimental value 0.35. As already said, the present linear theory gives an upper bound for Re^*, but has the advantage to account for the lateral confinement, whereas the 2-D theory of Müller et al. [16] not ($Ra^*_{\perp} = 1730$ instead of 1708 at $Re = 0$). Finally, any experiment with sustained noise (mechanical or thermal, say, e.g. by high power laser flashes) should only be compared with the present study.

To summarize, the 3-D linear theory allows one to determine the instability thresholds at $Re = 0$, and the transition $Ra^*_{//}$ between the basic flow and the $R_{//}$. However, the curve $Ra^*_{\perp}$ does correspond to a physically observed transition between the basic flow and the $R_{\perp}$, only in experiments (not available today) with continuous inlet perturbations of sufficient amplitude. Without sustained noise, it is preferable to use a convective weakly non-linear theory, even 2-D. Note that, to our knowledge, a convective stability theory, taking into account the lateral confinement of the channel, has never been developed for the present problem.

Table 8
Comparison of different values of k_x found in the literature with the values obtained by the present linear stability study

Reference	Methodology	Pr	B	Ra	Re	k_x
Luijkx et al. [24]	Shadowgraphy	450	5.25	4505	0.328×10^{-3}	2.856
				4505	0.95×10^{-3}	2.923
Present study	Linear stability			1770	23×10^{-3}	2.956
Schröder and Bülher [24]	3-D numerical simulation	530	4.1	7600	0.89×10^{-3}	2.596
				7600	$(1.42 \leq Re \leq 3) \times 10^{-3}$	2.732
Present study	Linear stability			1810	0.03	2.94
Nicolas et al. [33]	2-D numerical simulation	6.4	∞	1836	0.3	3.19
Present study	Linear stability	7		1794	2	3.081
Müller et al. [16]	2-D numerical simulation	1	∞	1903	2	3.155
				2420	4	3.307
Present study	Linear stability			1713	2	3.117
				1729	4	3.118

4.2. About the ratio of the transversal roll velocity to the average velocity of the basic flow: $(Vr/\langle\tilde{U}\rangle)^*$

It is well-known that the ratio $(Vr/\langle\tilde{U}\rangle)^*$ decreases linearly with Ra and is independent of Re [4,12,13,16,28,33]. In the present study, a relative independence of Re is also verified. Indeed, the variation of $(Vr/\langle\tilde{U}\rangle)^*$ is less than 4% when $0 \leq Re \leq Re^*$ (cf. Fig. 12 and Tables B1 and B2 in Appendix B). In Table 7, we compare values of $(Vr/\langle\tilde{U}\rangle)^*$ extracted from the literature with the results of the present work. The variation laws of $Vr/\langle\tilde{U}\rangle$ with Ra are given only for the results of the literature (experimental or non-linear theories). It can be noted that the linear stability accounts very well for the results of the literature at the critical point whatever Pr and B. Notice that, at $Pr = 6.4$, the influence of B is perfectly taken into account (compare the noticeable difference between $B = 3.6$ and $B \to \infty$).

4.3. About the wavelength of the transversal rolls: k_x^*

Very few results concerning the variation with Ra and Re of the wave number k_x of the 3-D transversal rolls are available in the literature. Indeed, the precise knowledge of k_x requires long computational domains or long experimental channels and, consequently, the numerical cost or the experimental difficulty are increased. Furthermore, the only available results when B is finite are for high Rayleigh numbers. In Table 8, we compare results from the literature with results of the linear stability for the same values of B and Pr, but at different Ra and Re. The orders-of-magnitude are in good agreement. However, it is difficult to go further into the comparison, because k_x depends on Ra and Re.

To conclude, the main interest of this study is to give numerical values of critical Rayleigh numbers, both for longitudinal and transversal rolls as a function of Re, Pr and B, taking for the first time into account the real 3-D character of the basic Poiseuille flow [Eq. (10)] and of the disturbances as well. In particular, even for transversal rolls, the three velocity components are non-vanishing. What is today missing, and of course needed, is a 3-D study of the convective instability ($Ra_\perp^{conv}$) as a function of the lateral confinement described by B, together with new experiments with sustained noise at the inlet.

Appendix A

Critical parameters for the 2-D transversal rolls in ducts of infinite transversal aspect ratios ($B \to \infty$) (Table A1).

Appendix B

Critical parameters as a function of Re, B and Pr for the 3-D transversal rolls ($k_x \approx 3$) in ducts of finite transversal aspect ratio ($1 \leq B \leq 5.2$) (Tables B1–B4).

Table A1
Critical Rayleigh number $Ra_\perp^*$ and critical wave number k_x^* as a function of Re, when $B \to \infty$, at $Pr = 10^{-6}$, 1, 7, 10 and 453

Re	$Pr = 10^{-6}$		$Pr = 1$		$Pr = 7$		$Pr = 10$		$Pr = 453$	
	$Ra_\perp^*$	k_x^*	$Ra_\perp^*$	k_x^*	$Ra_\perp^*$	k_x^*	$Ra_\perp^*$	k_x^*	$Ra_\perp^*$	k_x^*
0	1707.76	3.116	1707.76	3.116	1707.76	3.116	1707.76	3.116	1707.76	3.116
0.2	1707.76	3.116	1707.81	3.116			1709.49	3.116	3213.97	3.139
0.4	1707.77	3.116	1707.97	3.116			1714.67	3.113	4528.85	3.204
0.6	1707.79	3.116	1708.24	3.116			1723.26	3.109	5684.57	3.230
0.8	1707.81	3.116	1708.61	3.116			1735.20	3.104	6749.47	3.249
1	1707.84	3.116	1709.08	3.116	1729.61	3.107	1750.42	3.097	7755.20	3.263
1.2	1707.88	3.116	1709.67	3.116			1768.80	3.089	8720.17	3.273
1.4	1707.92	3.116	1710.35	3.117			1790.25	3.081	9655.88	3.282
1.6	1707.97	3.116	1711.15	3.117			1814.61	3.071	10,570.2	3.288
1.8	1708.03	3.116	1712.05	3.117			1841.77	3.061	11,468.9	3.294
2	1708.09	3.116	1713.05	3.117	1793.62	3.081	1871.57	3.051	12,356.3	3.299
3	1708.50	3.116	1719.67	3.117			2054.78	3.003	16,727.0	3.314
4	1709.08	3.116	1728.95	3.118			2281.36	2.972	21,188.8	3.308
6	1710.72	3.115	1755.51	3.120	2376.28	2.959	2805.05	2.977	31,366.0	3.195
8	1713.02	3.114	1792.83	3.123	2795.59	2.948	3373.72	3.025	44,741.6	2.937
10	1715.98	3.113	1841.05	3.126	3269.37	2.966	3987.50	3.055	62,927.7	2.512
20	1740.40	3.104	2252.38	3.155	6621.63	2.973	8574.21	2.885	100,168.1	6.928

Table B1
Critical parameters as a function of Re, for flows of 3-D horseshoe-shaped $R_{\perp}$, at $Pr = 10$ and $B = 1$, 2 and 5; $S = 48 \times 48$[a]

	$Pr = 10$				
	Re	$Ra^*_{\perp}$	k^*_x	σ^*_i	$(Vr/\langle\tilde{U}\rangle)^*$
$B = 1$ ($Ra^*_{//} = 2585.03$, $Re^* = 0.585$)	0.0	2369.07	3.170	0.0	
	0.1	2375.45	3.169	−4.552	1.436
	0.2	2394.51	3.164	−9.104	1.439
	0.3	2426.00	3.158	−13.664	1.442
	0.4	2469.46	3.150	−18.236	1.447
	0.5	2524.22	3.140	−22.840	1.455
	0.6	2589.30	3.131	−27.492	1.463
	0.8	2744.75	3.119	−37.052	1.485
	1.0	2920.52	3.119	−47.172	1.512
	1.5	3333.98	3.157	−75.040	1.585
	2.0	3640.49	3.157	−103.20	1.634
$B = 2$ ($Ra^*_{//} = 2013.24$, $Re^* = 1.196$)	0.0	1842.73	3.018	0.0	
	0.2	1861.46	2.993	−9.560	1.597
	0.4	1895.54	2.919	−18.956	1.624
	0.6	1924.86	2.845	−28.012	1.641
	0.8	1952.30	2.789	−36.808	1.650
	1.0	1981.60	2.739	−45.356	1.656
	1.2	2013.99	2.692	−53.612	1.660
	1.4	2049.63	2.643	−61.540	1.663
	1.6	2088.24	2.592	−69.108	1.666
	1.8	2129.40	2.539	−76.284	1.669
	2.0	2172.63	2.484	−83.040	1.671
$B = 5$ ($Ra^*_{//} = 1779.00$, $Re^* = 1.095$)	0.0	1712.09	3.038	0.0	
	0.2	1715.29	3.028	−8.928	1.474
	0.4	1723.29	3.013	−17.784	1.476
	0.6	1735.38	2.994	−26.536	1.477
	0.8	1751.08	2.971	−35.144	1.479
	1.0	1770.07	2.947	−43.600	1.479
	1.2	1792.24	2.922	−51.920	1.481
	1.4	1817.53	2.898	−60.120	1.482
	1.6	1845.85	2.875	−68.196	1.483
	1.8	1877.05	2.851	−76.148	1.484
	2.0	1910.97	2.828	−83.964	1.485

[a] The position of $Ra^*_{//}$ and Re^* is indicated by a horizontal separation line in each case.

Table B2
Critical parameters as a function of Re, for flows of 3-D horseshoe-shaped $R_{\perp}$, at $Pr = 453$ and $B = 5.2$; $S = 48 \times 48$[a]

	$Pr = 453$				
	Re	$Ra^*_{\perp}$	k^*_x	σ^*_i	$(Vr/\langle\tilde{U}\rangle)^*$
$B = 5.2$ ($Ra^*_{//} = 1770.05$, $Re^* = 0.02294$)	0.0	1711.45	3.044	0.0	
	0.01	1724.52	3.017	−20.400	1.493
	0.02	1757.28	2.971	−40.268	1.496
	0.03	1806.21	2.921	−59.504	1.499
	0.04	1869.75	2.873	−78.212	1.502
	0.1	2422.68	2.621	−181.228	1.526
	0.2	3333.73	2.793	−397.120	1.569
	1.0	7091.21	3.335	−2485.67	1.645
	2.0	8023.63	3.683	−5535.04	1.659

[a] The position of $Ra^*_{//}$ and Re^* is indicated by a horizontal separation line.

Table B3
Critical parameters at point ($Re = Re^*$; $Ra = Ra^*_{//}$) as a function of B, for flows of 3-D horseshoe-shaped $R_\perp$, at Pr = 1, 10, 100 and 453; $S = 12 \times 12$

	B	Re^*	k_x^*	σ_i^*	$(Vr/\langle\tilde{U}\rangle)^*$
$Pr = 1$	0.6	31.00	2.46	−98.80	1.30
	1.0	5.70	3.08	−23.89	1.36
	1.6	12.53	2.78	−51.75	1.49
	2.0	8.20	2.79	−33.57	1.47
	2.6	10.64	2.82	−43.05	1.44
	3.0	8.74	2.88	−35.34	1.40
	3.6	8.59	2.94	−34.97	1.38
	4.0	7.50	2.98	−30.48	1.36
	4.6	7.17	3.01	−28.96	1.34
	5.0	6.51	3.03	−26.18	1.33
	5.4	6.00	3.04	−24.03	1.32
$Pr = 10$	0.2	248.4	6.29	−24,527	1.57
	0.6	3.17	2.88	−130.60	1.43
	1.0	0.58	3.13	−26.70	1.46
	1.6	2.37	2.71	−108.51	1.69
	2.0	1.52	2.74	−69.06	1.65
	2.6	2.02	2.74	−89.05	1.61
	3.0	1.62	2.83	−72.44	1.58
	3.6	1.60	2.89	−71.30	1.54
	4.0	1.39	2.93	−61.87	1.52
	4.6	1.32	2.97	−58.58	1.49
	5.0	1.20	2.99	−52.83	1.47
	5.4	1.10	3.01	−48.42	1.46
$Pr = 100$	0.1	1774.5	8.48	-2.236×10^6	1.49
	0.6	0.316	2.94	−135.49	1.46
	1.0	0.058	3.13	−26.95	1.47
	1.6	0.247	2.72	−115.98	1.72
	2.0	0.157	2.75	−72.40	1.68
	2.6	0.208	2.74	−93.48	1.64
	3.0	0.167	2.83	−75.57	1.60
	3.6	0.164	2.89	−74.28	1.57
	4.0	0.142	2.93	−64.29	1.54
	4.6	0.135	2.97	−60.81	1.51
	5.0	0.122	2.99	−54.78	1.50
	5.4	0.112	3.01	−50.16	1.48
$Pr = 453$	0.1	1770.2	8.50	-1.014×10^7	1.49
	0.6	0.070	2.94	−135.90	1.46
	1.0	0.013	3.13	−26.97	1.48
	1.6	0.055	2.73	−116.31	1.73
	2.0	0.035	2.75	−75.52	1.75
	2.6	0.046	2.74	−93.63	1.64
	3.0	0.037	2.83	−75.97	1.61
	3.6	0.036	2.89	−74.38	1.57
	4.0	0.032	2.93	−64.37	1.54
	4.6	0.030	2.97	−60.88	1.52
	5.0	0.027	2.99	−54.84	1.50
	5.4	0.025	3.01	−50.22	1.48

Table B4
Critical parameters at point ($Re = Re^*$; $Ra = Ra^*_{//}$) as a function of Pr, for flow of 3-D horseshoe-shaped $R_\perp$ in ducts of aspect ratio $B = 2$ and 5.2; $S = 48 \times 48$

Pr	$B = 2$ ($Ra^*_{//} = 2013.24$)				$B = 5.2$ ($Ra^*_{//} = 1770.05$)			
	Re^*	k^*_x	σ^*_i	$(Vr/\langle\tilde{U}\rangle)^*$	Re^*	k^*_x	σ^*_i	$(Vr/\langle\tilde{U}\rangle)^*$
0.00001					17.02	3.080	-5.24×10^{-4}	1.000
0.0001					17.04	3.080	-5.26×10^{-3}	1.002
0.001					17.04	3.080	-5.28×10^{-2}	1.006
0.01					17.14	3.080	−0.532	1.008
0.05					16.58	3.086	−2.680	1.048
0.1					14.90	3.088	−4.996	1.086
0.2	19.70	2.515	−12.216	1.233				
0.3					10.08	3.039	−10.888	1.185
0.4					8.82	3.022	−12.996	1.219
0.5	10.48	2.740	−19.676	1.370	7.94	3.011	−14.880	1.245
0.6					7.28	3.003	−16.604	1.266
0.7					6.74	2.997	−18.204	1.287
1	6.98	2.737	−28.172	1.475	5.66	2.985	−22.404	1.326
2					3.84	2.966	−31.740	1.393
3	3.42	2.698	−44.180	1.596	2.90	2.958	−36.712	1.427
5	2.26	2.692	−49.360	1.623	1.924	2.954	−41.204	1.450
7	1.67	2.691	−51.792	1.646				
10	1.196	2.693	−53.436	1.659	1.018	2.953	−44.244	1.472
100	0.1231	2.700	−56.152	1.689	0.1039	2.955	−45.908	1.495
453	0.0272	2.701	−56.320	1.692	0.0229	2.956	−45.976	1.497
1000	0.0123	2.702	−56.352	1.692	1.039×10^{-2}	2.956	−45.988	1.497
10,000	1.233×10^{-3}	2.704	−56.424	1.693	1.039×10^{-3}	2.956	−45.996	1.498
100,000	1.233×10^{-4}	2.701	−56.356	1.693	1.039×10^{-4}	2.956	−45.996	1.498

References

[1] H. Bénard, D. Avsec, Travaux récents sur les tourbillons en bandes; applications à l'astrophysique et à la météorologie, J. Phys. et de Radium 9 (1938) 468–500.

[2] D. Brunt, Experimental cloud formation, in: Compendium of Meteorology, American Meteorological Society, Boston, 1951, pp. 1255–1262.

[3] M.E. Braaten, S.V. Patankar, Analysis of laminar mixed convection in shrouded arrays of heated rectangular blocks, Int. J. Heat Mass Transfer 28 (1985) 1699–1709.

[4] M. Hasnaoui, E. Bilgen, P. Vasseur, L. Robillard, Mixed convective heat transfer in a horizontal channel heated periodically from below, Num. Heat Transfer, Part A 20 (1991) 297–315.

[5] S.Q. Zhang, A.V. Tangborn, Flow regimes in two-dimensional mixed convection with spatially periodic lower wall heating, Phys. Fluids 6 (1994) 3285–3293.

[6] K.F. Jensen, E.O. Einset, D.I. Fotiadis, Flow phenomena in chemical vapor deposition of thin films, Annu. Rev. Fluid Mech. 23 (1991) 197–233.

[7] G. Evans, R. Greif, Thermally unstable convection with applications to chemical vapor deposition channel reactors, Int. J. Heat Mass Transfer 36 (1993) 2769–2781.

[8] N.K. Ingle, T.J. Mountziaris, The onset of transverse recirculations during flow of gases in horizontal ducts with differentially heated lower walls, J. Fluid Mech. 277 (1994) 249–269.

[9] J.-M. Luijkx, Influence de la présence de parois latérales sur l'apparition de la convection libre, forcée et mixte. Ph.D. thesis, Université d'état de Mons, Belgique, 1983.

[10] K.C. Chiu, J. Ouazzani, F. Rosenberger, Mixed convection between horizontal plates—II. Fully developed flow, Int. J. Heat Mass Transfer 30 (1987) 1655–1662.

[11] K.C. Chiu, F. Rosenberger, Mixed convection between horizontal plates—I. Entrance effects, Int. J. Heat Mass Transfer 30 (1987) 1645–1654.

[12] M.T. Ouazzani, J-P. Caltagirone, G. Meyer, A. Mojtabi, Etude numérique et expérimentale de la convection mixte entre deux plans horizontaux à températures différentes, Int. J. Heat Mass Transfer 32 (1989) 261–269.

[13] M.T. Ouazzani, J.-K. Platten, A. Mojtabi, Etude expérimentale de la convection mixte entre deux plans horizontaux à températures différentes—II, Int. J. Heat Mass Transfer 33 (1990) 1417–1427.

[14] M.T. Ouazzani, J.-K. Platten, A. Mojtabi, Intermittent patterns in mixed convection, Applied Scientific Research 51 (1993) 677–685.

[15] M.T. Ouazzani, J.-K. Platten, H.W. Müller, M. Lücke, Etude de la convection mixte entre deux plans horizontaux à des températures différentes—III, Int. J Heat Mass Transfer 38 (1995) 875–886.

[16] H.W. Müller, M. Lücke, M. Kamps, Transversal convection patterns in horizontal shear flow, Physical Review A 45 (1992) 3714–3725.

[17] W. Velte, Zür Stabilität der Strömung in einem horizontalen Rohr bei ungleichmäßig erwärmter Wand, Z. Angew. Math. Phys. 13 (1962) 591–600.
[18] R. Sani, Note on flow instabilities in heated ducts, Z. Angew. Math. Phys. 15 (1964) 381–387.
[19] Y. Mori, Y. Uchida, Forced convective heat transfer between horizontal flat plates, Int. J. Heat Mass Transfer 9 (1966) 803–817.
[20] K.S. Gage, W.H. Reid, The stability of thermally stratified plane Poiseuille flow, J. Fluid Mech. 33 (1968) 21–32.
[21] J.-K. Platten, A variational formulation for the stability of flows with temperature gradients, Int. J. Engng Sci. 9 (1971) 855–869.
[22] H.B. Squire, On the stability for three-dimensional disturbances of viscous fluid flow between parallel walls, Proc. Roy. Soc. London, A 42 (1933) 621–628.
[23] J.-K. Platten, J.-C. Legros, Convection in Liquids, Springer Verlag, Berlin, Heidelberg, 1984 Chaps 6 and 8.
[24] J.-M. Luijkx, J.-K. Platten, J.-C. Legros, On the existence of thermoconvective rolls, transverse to a superimposed mean Poiseuille flow, Int. J. Heat Mass Transfer 24 (1981) 803–817.
[25] C.H. Yu, M.Y. Chang, T.F. Lin, Structures of moving transverse and mixed rolls in mixed convection of air in a horizontal plane channel, Int. J. Heat Mass Transfer 40 (1997) 333–346.
[26] H.R. Brand, R.J. Deissler, G. Ahlers, Simple model for the Bénard instability with horizontal flow near threshold, Physical Review A 43 (1991) 4262–4268.
[27] H.W. Müller, M. Tveitereid, S. Trainoff, Rayleigh–Bénard problem with imposed weak through-flow: two coupled Ginzburg–Landau equations, Physical Review E 48 (1993) 263–272.
[28] E. Schröder, K. Bühler, Three-dimensional convection in rectangular domains with horizontal throughflow, Int. J. Heat Mass Transfer 38 (1995) 1249–1259.
[29] M.Y. Chang, C.H. Yu, T.F. Lin, Flow visualization and numerical simulation of transverse and mixed vortex roll formation in mixed convection of air in a horizontal flat duct, Int. J. Heat Mass Transfer 40 (1997) 1907–1922.
[30] C.H. Yu, M.Y. Chang, C.C. Huang, T.F. Lin, Unsteady vortex roll structures in a mixed convective air flow through a horizontal plane channel: a numerical study, Int. J. Heat Mass Transfer 40 (1997) 505–518.
[31] D. Roth, P. Büchel, M. Lücke, H.W. Müller, M. Kamps, R. Schmitz, Influence of boundaries on pattern selection in through-flow, Physica D 97 (1996) 253–263.
[32] X. Nicolas, P. Traore, A. Mojtabi, J.-P. Caltagirone, Augmented Lagrangian method and open boundary conditions in 2-D simulation of Poiseuille–Bénard channel flow, Int. J. Number. Meth. Fluids 25 (1997) 265–283.
[33] X. Nicolas, A. Mojtabi, J.-K. Platten, Two dimensional numerical analysis of the Poiseuille–Bénard flow in a rectangular channel heated from below, Physics of Fluids 9 (1997) 337–348.
[34] J.-M. Luijkx, J.-K. Platten, On the onset of free convection in a rectangular channel, J. Non-Equilibrium Thermodyn. 6 (1981) 141–158.
[35] B.T. Smith, J.M. Boyle, J.J. Dongarra, B.S. Garbow, Y. Ikebe, V.C. Klema, C.B. Moler, Matrix eigensystem routines—Eispack Guide, Lecture Notes in Computer Sciences, Springer-Verlag, vol. 6, 1976.
[36] I. Catton, The effect of insulating vertical walls on the onset of motion in a fluid heated from below, Int. J. Heat Mass Transfer 15 (1972) 665–672.
[37] C.S. Yi, Thermal instability of viscous fluids, Quart. J. Appl. Math. 17 (1959) 25–42.
[38] R.J. Deissler, Spatially growing waves, intermittency, and convective chaos in an open-flow system, Physica D 25 (1987) 233–260.
[39] P. Huerre, Spatio-temporal instabilities in closed and open flows, in: E. Tirapegui, D. Villaroel (Eds.), Instabilities and Nonequilibrium Structures, Reidel, Dordrecht, 1987, pp. 141–177.
[40] S.S. Chen, A.S. Lavine, Laminar, buoyancy induced flow structures in a bottom heated, aspect ratio 2 duct with throughflow, Int. J. Heat Mass Transfer 39 (1996) 1–11.